

The Dynamics of Circulations within the Trailing Stratiform Regions of Squall Lines. Part I: The 10–11 June PRE-STORM System

WILLIAM A. GALLUS, JR.* AND RICHARD H. JOHNSON

Department of Atmospheric Science, Colorado State University, Fort Collins, Colorado

(Manuscript received 23 February 1994, in final form 4 August 1994)

ABSTRACT

A dynamic version of the two-dimensional kinematic cloud model of Rutledge and Houze has been developed to investigate the effects of microphysics on circulations within the stratiform regions of mesoscale convective systems. The design of the model allows for specified inputs of hydrometeors, water vapor, and heat from the convective line. The stratiform region of the 10–11 June 1985 PRE-STORM squall line is simulated, with initialization based upon appropriate soundings, heat budgets, and 1D cumulonimbus model results.

The model accurately simulates the evolution of the stratiform rain area. Significant ascent occurs in the stratiform region where in situ condensate production contributes increasingly to the surface rainfall, reaching 65% of the total in the mature stage and averaging 44% over the entire simulation. The ratio of condensate produced within the mesoscale updraft to that advected from the convective line generally agrees with water budgets from other studies. Simulated horizontal flows agree qualitatively with observations and include a sloping rear-inflow jet that develops with peak speeds approaching those observed. A transition zone, marked by a minimum in surface precipitation separating the convective and stratiform regions, broadens over time, especially late in the simulation after leading convective elements weaken.

The model has several limitations: it is 2D and neglects radiation and large-scale baroclinicity. As in previous 2D models, surface rainfall is underestimated, implying the importance of 3D convergent forcing of strong ascent in the anvil cloud. Ascent is underestimated near stratiform cloud top, indicating that cloud-top radiative effects are possibly important in generating circulations there. Strong rear-inflow is restricted to within 100 km of the convective line, suggesting that rear inflow at higher levels far to the rear of the squall line (which occurred in the 10–11 June case) may require large-scale baroclinicity.

1. Introduction

Observational studies have long shown that convective cells can organize into long lines extending over distances of several hundred kilometers, with large regions of stratiform precipitation trailing the intense convection (e.g., Newton 1950). These systems, known as squall lines, have been commonly divided into three regions based partially on the characteristics of surface rainfall within them: the leading convective line, a band of intense rainfall 10–50 km wide; the transition zone, a region of little or no surface precipitation; and the stratiform region, an area 50–150 km wide of rather uniform rainfall (Smull and Houze 1985).

A front-to-rear (FTR) jet is initiated or enhanced by the convergence of horizontal momentum transported

vertically by convective motions in the leading convective line (Smull and Houze 1987a). Small-scale pressure perturbations induced at midlevels in the convective line assist in the momentum transport (LeMone 1983). The FTR jet transports significant amounts of hydrometeors rearward, establishing a broadening anvil cloud and stratiform precipitation region behind the system (Rutledge 1986; Rutledge and Houze 1987). Mesoscale ascent, generally on the order of tens of centimeters per second, develops behind the convective line and also contributes to the stratiform rainfall by allowing the growth of the hydrometeors through a seeder–feeder type process. Water budgets have shown that the amount of surface rainfall due to the in situ production of condensate can vary from 25% (Gamache and Houze 1983) to 80% (Rutledge and Houze 1987). The ascent in the stratiform region may be due to several processes. High θ_e air detrained from active and dissipating convective towers is slightly positively buoyant and, when transported rearward, will ascend (Knupp and Cotton 1987). Latent heat released through condensation, fusion, and deposition within the anvil cloud will also encourage ascent (Houze 1982; Churchill and Houze 1984). Roux (1988) has argued that the increase in effective buoyancy due to the fallout

* Current affiliation: UCAR visiting scientist, National Meteorological Center, Camp Springs, MD.

Corresponding author address: Dr. William A. Gallus, Jr., World Weather Building, National Meteorological Center, 5200 Auth Road, Camp Springs, MD 20746.

of precipitation can maintain the mesoscale updraft. Longwave radiative transfer may enhance the ascent by destabilizing the stratiform cloud layer (Webster and Stephens 1980; Tao et al. 1991).

The transition zone, which separates the convective line and stratiform regions, often develops after convection has occurred for several hours and it later broadens, especially after the convective line weakens. The orientation of the transition zone is usually similar to that of the convective line, implying some dependence on processes that occur in the convective region (Leary and Rappaport 1987). The transition zone has been attributed to both fallspeed sorting—heavier hydrometeors falling out within the convective line, while lighter ones are carried significantly farther rearward into the stratiform region (Smull and Houze 1987a)—and enhanced subsidence, which increases sublimation and evaporation (Smull and Houze 1985). Biggstaff and Houze (1993) find that a combination of kinematic and microphysical processes lead to the transition zone. The most important factor is the relative minimum in aggregation just above the melting level in the transition zone. The enhanced subsidence has relatively little effect on radar reflectivities, except at midlevels where it has some role in reducing aggregation.

A strong current of rear-to-front (RTF) flow known as the rear-inflow jet (Smull and Houze 1985) often occurs within squall lines and has also been attributed to one or more of several different processes involving 1) the stratiform region, 2) the convective line, and 3) the environmental flow. Within the stratiform region, microphysical cooling due to sublimation and evaporation of falling rain drives a mesoscale downdraft with magnitudes similar to those of the updraft (Zipser 1969). The cooling at low levels with microphysical heating aloft induces a midlevel mesowave with pressure gradients that, in cases like the 10–11 June PRE-STORM (Preliminary Regional Experiment for STORM-Central) squall line, are of sufficient strength to explain the observed amplitude of the jet (Gallus and Johnson 1992).

Buoyancy gradients due in part to processes within the convective line also influence the jet (Smull and Houze 1985; Lafore and Moncrieff 1989; Weisman 1992). In some squall lines, these processes may be of primary importance (Klimowski 1994). Zhang and Gao (1989) have attributed the portion of the jet descending to the surface near the convective line in the 10–11 June system to convective-scale downdrafts. Farther to the rear of the squall line at high levels, large-scale baroclinicity may induce RTF flow (Zhang and Gao 1989). Schmidt and Cotton (1990) argue that initial descent of the rear-inflow jet from high levels may be due to blocking from the upper-level mesowave, enhanced by interacting gravity wave circulations. In some systems, like the 10–11 June case, the rear-inflow jet gradually descends from high elevations at the rear of the anvil cloud (8 or 9 km) to near the surface in the

convective line region. In other systems, like the 3–4 June PRE-STORM case, the rear-inflow jet descends abruptly at low levels at the back of the stratiform region as though it were blocked (Stumpf et al. 1991).

Squall lines with extensive trailing stratiform regions have been successfully simulated with both mesoscale and cloud-scale models (e.g., Zhang and Gao 1989; Fovell and Ogura 1988). In general, these simulations have looked at the entire system. The models have often not concentrated on the differing roles of separate microphysical processes or distinguished between convective line processes and those taking place within the stratiform region. Some of the exceptions include the work of Tao et al. (1991), who studied the water budget of the stratiform region, or Stensrud et al. (1991) and Szeto et al. (1988b), who investigated the dynamic effects of deposition and sublimation, and melting and evaporation, respectively.

The objective of this study is to develop a two-dimensional model to investigate the role of microphysics in developing and sustaining mesoscale circulations within the trailing stratiform region. The model domain is restricted to the stratiform region, reducing computational costs and permitting many sensitivity tests to be run. The model is applied to the well-observed 10–11 June PRE-STORM case (e.g., Johnson and Hamilton 1988; Rutledge et al. 1988; Zhang et al. 1989; Zhang and Gao 1989; Gallus and Johnson 1991; Biggstaff and Houze 1993). In Part I of this study, the following questions are investigated:

- How do the rainfall and microphysics in the stratiform region evolve as hydrometeors advect rearward from the convective line?
- Are the heating aloft and ensuing cooling below from sublimation, melting, and evaporation of these hydrometeors sufficient to induce a rear-inflow jet of the observed magnitude apart from baroclinicity?

Part II will investigate the sensitivity of stratiform region circulations to environmental conditions. In addition, sensitivity tests will show to what extent the advection of hydrometeors and associated latent heat release due to vapor deposition, fusion, and condensation contribute to upward motion in the stratiform region. A subsequent paper will apply the model to a case where the rear-inflow jet was blocked to determine whether microphysical processes alone can force strong subsidence and an intense wake low at the rear of the stratiform region.

2. Description of the numerical model

There are obviously trade-offs associated with the modeling approach used in this study. While the difficult problem of simulating a realistic convective line is avoided, realistic representation of its effects on the stratiform region, via hydrometeor, heat, and momen-

tum transports, must be included. Treatments of these processes will be discussed later.

In essence, the model developed is a dynamic version of the detailed kinematic microphysical model used by Rutledge (1986) and Rutledge and Houze (1987). The microphysical parameterization is described in Rutledge and Hobbs (1983, 1984). The model initialization is based on PRE-STORM data for the 10–11 June squall line case, and convective inputs are based upon actual observations during the full lifetime of the system as much as possible. The model, with its expanded microphysical scheme, elaborates on the stratiform simulations of Szeto et al. (1988b) and Stensrud et al. (1991).

a. Model equations

Because the model used in this study is applied to the stratiform region of a rather linear squall line and Redelsperger and Lafore (1988), among others, have found little difference between the 2D and 3D physics of most linear squall lines, the model is chosen to be two-dimensional. This model uses the “deep anelastic” equations formulated by Ogura and Phillips (1962) and ignores variations in the predicted variables in the y direction or along the squall line. The equations governing the dynamics are therefore very similar to those expressed in Orlanski and Ross (1977) and Szeto et al. (1988a), with flat terrain. Radiation is excluded. Longwave radiative effects have been shown to increase surface rainfall, and the strength of circulations by roughly 15% in the stratiform region (e.g., Tao et al. 1993), yet the exclusion of radiation does not seem to change simulations qualitatively. (The exclusion of radiation is therefore felt to be an acceptable simplification in the model that significantly reduces computation costs.) For the simulations performed, the Coriolis parameter f is set to zero so that the model is truly two-dimensional. Fovell (1991) suggested that the lack of Coriolis force has no significant impact for simulations of 4 hours or less. It may be important after 6 hours, and it seems to produce a braking affect on circulations after 10 hours. The simulations discussed in this study were only integrated to 7 hours or less. Surface sources and sinks of heat are neglected; the 10–11 June system occurred at night over land, so the exclusion should be acceptable. However, moist processes are permitted in the model, and precipitation drag is included.

The model equations are formulated using the streamfunction ψ and y -component vorticity η for motion in the x – z plane. The resulting equation set is

$$\begin{aligned} \frac{\partial \eta}{\partial t} = & J(\psi, \alpha_0 \eta) + f \frac{\partial v}{\partial z} - \frac{g}{\theta_0} \frac{\partial \theta}{\partial x} + \frac{\partial}{\partial x} \left(\nu_H \frac{\partial \eta}{\partial x} \right) \\ & + \frac{\partial}{\partial z} \left(\nu_z \frac{\partial \eta}{\partial z} \right) - gE \frac{\partial q_v}{\partial x} + g \frac{\partial q_T}{\partial x} \quad (1) \end{aligned}$$

$$\begin{aligned} \frac{\partial v}{\partial t} = & \alpha_0 J(\psi, v) - f \left(\frac{\alpha_0 \partial \psi}{\partial z} - U \right) \\ & + \frac{\partial}{\partial x} \left(\nu_H \frac{\partial v}{\partial x} \right) + \frac{\partial}{\partial z} \left(\nu_z \frac{\partial v}{\partial z} \right) \quad (2) \end{aligned}$$

$$\begin{aligned} \frac{\partial \theta}{\partial t} = & \alpha_0 J(\psi, \theta) - v \frac{\partial \theta_g}{\partial y} + \frac{\partial}{\partial x} \left(K_H \frac{\partial \theta}{\partial x} \right) \\ & + \frac{\partial}{\partial z} \left(K_z \frac{\partial \theta}{\partial z} \right) + \frac{\theta_0}{C_p} \frac{Q^*}{T_0} \quad (3) \end{aligned}$$

$$\eta = \frac{\partial}{\partial x} \left(\alpha_0 \frac{\partial \psi}{\partial x} \right) + \frac{\partial}{\partial z} \left(\alpha_0 \frac{\partial \psi}{\partial z} \right) \quad (4)$$

$$u = \alpha_0 \frac{\partial \psi}{\partial z} \quad (5)$$

$$w = -\alpha_0 \frac{\partial \psi}{\partial x}, \quad (6)$$

where ν_H and ν_z are the horizontal and vertical eddy viscosity, K_H and K_z are the horizontal and vertical eddy diffusivity, E is the constant 0.61, q_T is the total hydrometeor mixing ratio, q_v the water vapor mixing ratio, α_0 the initial horizontally averaged value of specific volume, θ_g the initial geostrophic potential temperature (which can nominally vary in the y direction), and C_p the heat capacity of dry air. The notation is generally conventional, and a full list of symbols appears in appendix A. The term Q^* represents all diabatic heating sources; in total, 18 phase changes contribute to this term. It is computed using the bulk water parameterized microphysical equations of Rutledge and Hobbs (1983, 1984), which were based upon the work of Lin et al. (1983). The model allows for six classes of water substance, including three ice phase classes. Several revisions of the microphysical equations are presented in appendix B, although the full scheme is discussed in Rutledge and Hobbs (1983, 1984). The advective effects in these equations are represented in Jacobian form.

b. Numerical aspects

The system of partial differential equations (1)–(3) is solved using the leapfrog finite-differencing scheme. Spatial derivatives are represented with centered differences except at the boundaries where one-sided differences must be used. The diffusion terms are lagged by one time step (as in Szeto et al. 1988a). Finite differencing of the Jacobian terms is done using the Arakawa (1966) formulation to minimize computational instability. The presence of the Laplacian on the right-hand side of the vorticity equation means that an elliptic equation must be solved to advance the equation set in time. The time step used in the model is 15 seconds. To suppress the time mode splitting associated with the

leapfrog scheme, a Robert frequency filter (Asselin 1972) of 0.18 is applied at every time step. Simulations are integrated for 7 hours.

The model domain is resolved by a uniformly spaced nonstaggered grid system with a 5-km Δx and 400-m Δz . The grid network consists of 65 points in the x direction and 41 in z , with a lower boundary at 500 m [the approximate average surface elevation of the PRE-STORM project domain (Johnson and Hamilton 1988)] and an upper boundary at 16.5 km. The model results are not particularly sensitive to the domain size and grid spacing, a common feature in mesoscale simulations of convection (e.g., Dudhia et al. 1987; Hsie et al. 1984; Schmidt and Cotton 1990). The insensitivity to domain size is probably due in part to the open radiative lateral boundary conditions (Orlanski 1976) and also to the rather smooth motions that were taking place within the domain.

c. Microphysical parameterization

Heymsfield and Hjermfelt (1984) and Rutledge (1986) have shown that ice, snow, and graupel are all present within convective cores, all can be distinguished advecting to the rear of a convective line, and all phase changes involving vapor, ice, and liquid within the stratiform anvil are believed to be important in generating circulations there. In general, the more ice classes used in a parameterization scheme, the better the simulations obtained (McCumber et al. 1991). This model uses a microphysical scheme that includes all water phase changes and allows interaction between six different water classes.

As in Rutledge and Hobbs (1983, 1984), the particles constituting the cloud water and cloud ice fields are assumed to be monodisperse with sizes of rain, snow, and graupel distributed continuously according to an inverse exponential distribution. The Rutledge and Hobbs parameters for graupel are actually more representative of aggregates than graupel, and these parameters are appropriate for this model since graupel are relatively rare rearward of the transition zone in actual squall-line systems (McCumber et al. 1991). The graupel is assumed to be quasispherical with a density of 0.4 g cm^{-3} . The slope intercept values $N_{0\alpha}$ are held constant, and the slope factors therefore vary according to the mixing ratios of the hydrometeors present. Cotton and Anthes (1989) have shown that the assumption of a constant slope intercept value, though commonly used, may not be valid, particularly in regions where the size distributions may change significantly due to breakup; however, since this model is applied to the rather tranquil conditions of the stratiform rain regions of squall lines, where vertical velocities generally remain small, it was felt that a constant intercept value was a better assumption than a constant slope value. The slope factors are as in Rutledge and Hobbs (1983, 1984), but with modifications to agree

with Locatelli and Hobbs (1974) as presented in Potter (1991) (See appendix B).

The advection terms are computed using the positive definite scheme of Bott (1989), which produces only small numerical diffusion.

d. Subgrid-scale turbulence parameterization

A first-order closure is used for the Reynolds stress terms. Turbulent fluxes of momentum and heat are parameterized using an eddy viscosity scheme that accounts for increased turbulence production in regions of convective instability. The eddy diffusivity in this scheme is defined as in Orlanski and Ross (1973, 1977) and Szeto et al. (1988a). The constant c is set to 0.5 in this study. When tested, the model showed little change due to variations of c within the range of 0.1 to 0.75. Horizontal diffusion is included in the model as an additional source of numerical smoothing, and the horizontal exchange coefficients are related to the vertical values as in Szeto et al. (1988a). The constant D is set at 5.0 and K_{z0} , the constant background value of vertical eddy diffusivity, is set at $0.6 \text{ m}^2 \text{ s}^{-1}$. In general, simulations were insensitive to variations of K_{z0} from 0.3 to 4.0.

e. Boundary conditions

Because of computational constraints, the domain size chosen ($\sim 300 \text{ km}$) is not large enough to fully include a large mesoscale convective system (MCS), so open radiative boundary conditions are used (Orlanski 1976). The domain travels with a convective system so that one lateral boundary always stays at the "interface" between a convective line region and a stratiform region (Fig. 1). FTR flow is prescribed initially, and the model is driven by the rearward transport of hydrometeors from the convective line region so that inflow conditions occur within the cloud layer on this boundary. Any transition zone must develop within the model domain, and hydrometeors move rearward as they fall through high levels of this zone. Similar to Orlanski (1976), a pure outflow gravity wave speed is assumed at both lateral boundaries for certain variables. The use of this outflow speed for all dynamic variables results in more realistic results and is supported by Durran et al. (1993).

Hydrometeor contents on the inflow boundary are prescribed according to a set pulsing rate of 30 minutes. As will be discussed later, this pulsing rate was necessary so that the amount of water mass entering the stratiform region agreed with the water budget of this case by Gallus and Johnson (1991, hereafter GJ). In addition, modeling studies of Dudhia et al. (1987), LaFore and Moncrieff (1989), and Fovell and Ogura (1988) showed that convection within simulated MCSs typically pulsed with a frequency of roughly 15–30 minutes. Observations also imply this pulsing of the

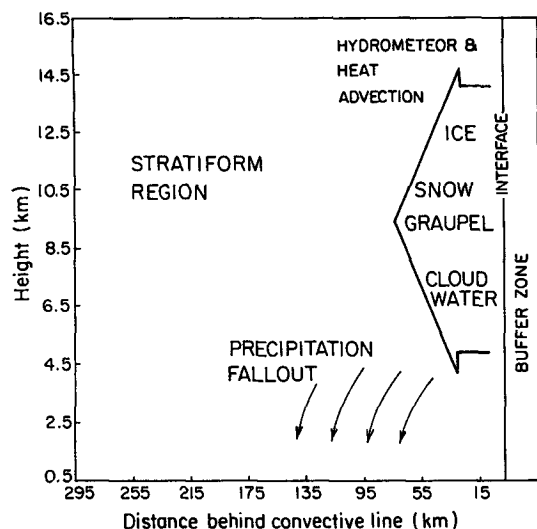


FIG. 1. Schematic of the model domain depicting important driving processes to the circulations that may develop. Back edge of convective line is assumed to lie at the right boundary. Height expressed in kilometers MSL on this figure and all similar figures.

cumulus towers, which are believed to be left behind, and drift in a relative sense into the stratiform region of these large systems. Therefore, the hydrometeor advection into the stratiform region will realistically not be continuous but will vary over time. A sinusoidal variation is assumed for simplicity in this model.

A "buffer zone" is used at the inflow boundary so that the effects of the microphysical processes can be smoothed slightly in that region (see Fig. 1). The buffer zone consists of five grid points where the microphysical rates decrease linearly toward the right boundary. This region is therefore "transparent" to the hydrometeors passing through it, which are not permitted to fall. The buffer zone (not shown in most figures) helps slightly to smooth the circulation at the inflow boundary.

Because the buoyancy gradient at the back edge of the convective line may strongly influence the rear-inflow jet (Weisman 1992), diabatic heating is prescribed in the buffer zone using values from GJ. Thermodynamic conditions at the right boundary are relaxed toward initial conditions after the convective influence of heating and hydrometeor advection diminishes. The effects of momentum transport from the convective line have been examined using profiles from the momentum budget of Gallus and Johnson (1992). Since model results were not significantly affected by momentum transports, their effects are neglected.

A free-slip rigid lid is used for the upper and lower boundaries, and the lapse rate is held at its initial value. Newtonian damping is applied to the upper three layers (1.2 km) to absorb vertically propagating gravity waves.

f. Initial conditions

Ambient FTR flow exists at all levels initially, with one maximum near the surface and a stronger one at high levels (Fig. 2) with no vertical motion. A minimum in FTR flow exists near the melting level (roughly 4 km). This wind profile resembles a mix between that of the presquall environment and the developing convective line region (see Figs. 2, 13; Gallus and Johnson 1992). Lapse rates are nearly moist adiabatic. The temperature field is horizontally homogeneous above the melting level, but a 3 K cold pool is initialized below that level in the 75 km nearest the right boundary to represent the region influenced by cold downdrafts from the newly developed convective line (see Fig. 2). Model sensitivity to these initial conditions will be discussed in Part II.

Saturated conditions with respect to water exist at the right boundary within the layer in which cloud water advects into the domain from the convective line (Fig. 3). Humidities decrease toward the left boundary to just under 40% at the left boundary in the layer 3.7–10.5 km. It was found that a horizontally homogeneous initialization of the vapor field using the rather dry values found at the left of the domain eventually produced similar model results as the horizontally varying method used, with the main difference being a slight delay in the horizontally homogeneous case.

Because observational hydrometeor mixing ratio data to be used as input on the right boundary were not readily available for the 10–11 June case, the one-dimensional, Eulerian cumulonimbus model of Ferrier and Houze (1989), applied to this case by Rickenbach

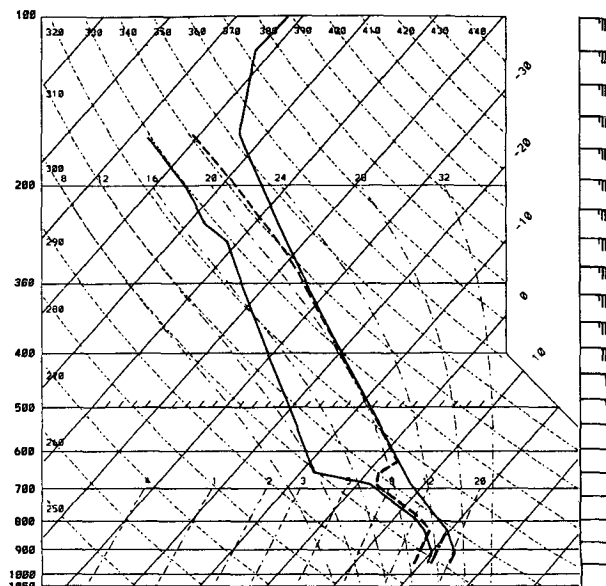


FIG. 2. Initial thermodynamic profiles with left boundary values solid and right boundary values dashed. Ambient wind is horizontally homogeneous and can be seen at the right of each skew T .

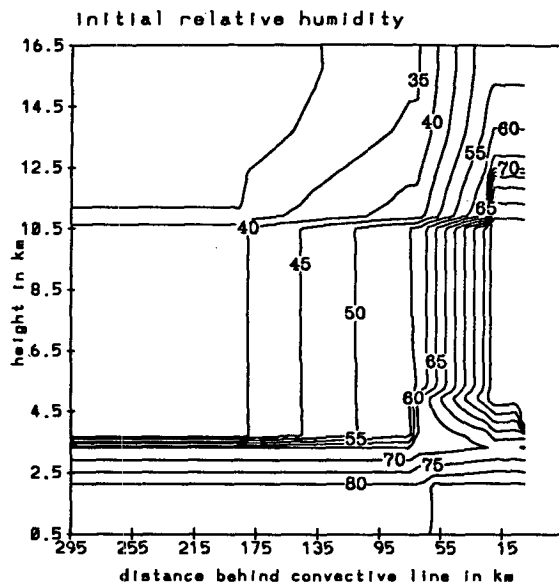


FIG. 3. Initial relative humidity field with respect to water in the model domain. Contour interval is 5%.

(1990), was used. Rickenbach initialized the Ferrier and Houze model with the Enid, Oklahoma, 2330 UTC sounding and predicted vertical profiles of reflectivity, which were compared with observed profiles over a 3-hour period corresponding to the mature phase of the convective line when the stratiform region was undergoing its development. The model profile of reflectivity most closely matching the observed reflectivity was used at several times to provide an accurate estimate of the hydrometeor contents within the squall line convection. An average value of the mixing ratios of snow, graupel, and cloud ice diagnosed by Rickenbach over the 3-hour period is used as input for the simulation in this study (Fig. 4).

Peak snow and graupel mixing ratios are similar to the aircraft measurements within Oklahoma convection (Heymsfield and Hjermfelt 1984) used in the midlatitude squall line study of Rutledge and Houze (1987). Peak cloud ice mixing ratios are two or three times greater than in the Rutledge and Houze case. Because vertical profiles of cloud water at the back of the convective cores were not available in the Rickenbach (1990) study, values from Rutledge and Houze (1987) are used to initialize the current simulation.

The pulsing of these hydrometeor contents led to better agreement with the observed hydrometeor advection (GJ). The diagnosed values described above, if permitted to enter the domain at a constant rate, allowed too much hydrometeor mass to enter the stratiform region over a given time period. A simulation run without pulsing but allowing the same integrated water mass to enter the domain over time yielded quantitatively different results, but without qualitative changes.

Peak values of ascent, descent, and surface rainfall were significantly diminished, but the overall evolution of the circulations was similar.

A significant amount of heat can be transported vertically and rearward by intense convection; additionally, circulations produced by this heating may interact with the microphysically induced circulations in the anvil cloud. To investigate these effects, diabatic heating rates are prescribed over a portion of the buffer zone 15-km wide, and the rates pulse with the same frequency as the hydrometeors. The heating profile is roughly sinusoidal with a peak of 12 K h^{-1} at 6.5 km. Cooling is restricted to the lowest kilometer of the buffer zone, with a peak value of 3 K h^{-1} .

3. Observations of the 10–11 June squall line

The 10–11 June squall line began as broken line convection (Bluestein and Jain 1985) over southwestern Kansas and the Oklahoma panhandle ahead of a cold front prior to 2100 UTC 10 June. Radar reflectivities in the convective line peaked within an hour after 0100 UTC (Fig. 5a, from Rutledge et al. 1988), as the stratiform region was growing significantly in area and intensity and a transition zone was developing. The stratiform region appeared to reach its maximum intensity within an hour after 0400 UTC (Fig. 5b) with averaged surface rainfall rates around 3 mm h^{-1} (GJ) and peak values as high as 6 mm h^{-1} in areas with reflectivity exceeding 35 dBZ. After the peak rainfall oc-

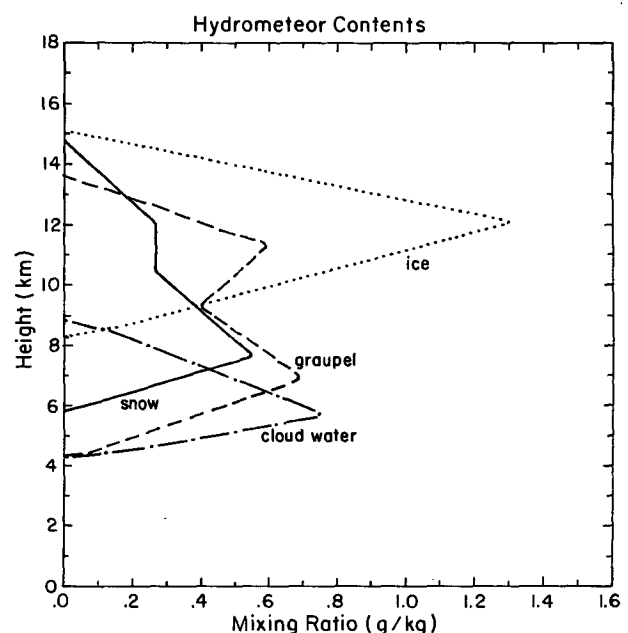
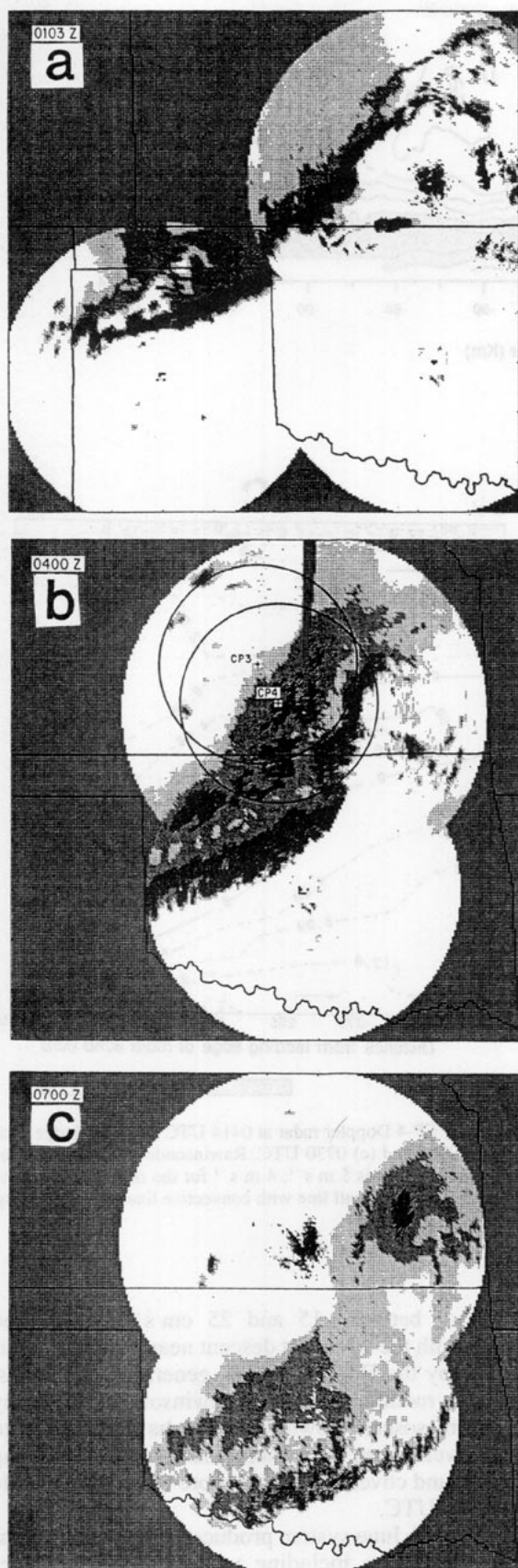


FIG. 4. Hydrometeor contents within convective line cells. Profiles of snow (solid), graupel (dashed), and cloud ice (dotted) are averages taken from Rickenbach (1990). Cloud water (dash-dotted) is taken from Rutledge and Houze (1987).



curred, the stratiform region began dissipating (Fig. 5c) and the transition zone broadened markedly, as the convective line moved with a much faster speed (over 15 m s^{-1}) than the stratiform region (roughly 8 m s^{-1}).

During the mature stage of the system, three primary circulation features existed (Fig. 6): an ascending FTR jet, a descending rear-inflow jet, and a return FTR flow near the surface. Doppler data from CP-4 (Rutledge et al. 1988) at 0414 UTC (Fig. 6a) and rawinsonde data (GJ) at 0300 and 0730 UTC (Figs. 6b,c) show the axis of the FTR jet extending from around 5–7 km at the back of the convective line region, to 9–10 km at the back of the region of surface stratiform rain, to as high as 11 or 12 km at the rear of the cloud. Peak storm-relative magnitudes were generally over 20 m s^{-1} , reaching 30 m s^{-1} at 0300 UTC (Fig. 6b).

Below the FTR jet, a strong rear-inflow jet with peak values as large as 15 m s^{-1} gradually descended through the system, with the axis of the jet generally near or below the melting level in the stratiform rain region. At the rear of the system, RTF flow extended to as high as 8 km. The RTF jet appeared to intensify and descend more closely to the surface between 0300 and 0730 UTC (Figs. 6b,c). Beneath the rear inflow jet, another FTR current existed near the surface, the result of an overturning downdraft beneath the stratiform anvil cloud.

Vertical motion as determined from both Doppler and rawinsonde data is shown in Fig. 7 (from Rutledge et al. 1988; Gallus and Johnson 1991). EVAD (extended velocity-azimuth display) analyses indicate a transition from low-level descent to ascent aloft between the melting level, 4.1 km, and 6.5 km (Figs. 7a,b). The depth of the mesoscale downdraft varies significantly between the CP3 and CP4 sites, which were aligned nearly perpendicular to the squall line motion 45 km apart. Peak descent of $60\text{--}75 \text{ cm s}^{-1}$ was located near the melting level at CP3 after 0300 UTC, but around 2.5 or 3 km at CP4. Strongest ascent aloft was generally between $50\text{--}60 \text{ cm s}^{-1}$, and the level of peak ascent varied from 8 to 12 km.

The evolution of vertical motion can be seen in the rawinsonde-derived ω field at 0300 (Fig. 7c), 0600 (Fig. 7d), and 0730 UTC (Fig. 7e). Aliasing of data between the convective line and stratiform regions is a significant problem, particularly in the 0300 and 0600 UTC data. In addition, the truncation of soundings in the leading part of the stratiform region can degrade ω estimates. The peak ascent in the stratiform region at 0730 UTC, when aliasing was less of a problem, was

FIG. 5. Composite low-level echo patterns from the AMA, ICT, and OKC WSR-57 10-cm radars for (a) 0103, (b) 0400, and (c) 0700 UTC (taken from Rutledge et al. 1988). Reflectivity of 15–25 dBZ shown with light stippling; 25–35 dBZ, heavy stippling; 35–50 dBZ, hatching; and ≥ 50 dBZ, solid. Circles at 0400 UTC show the coverage of CP-3 and CP-4 radars.

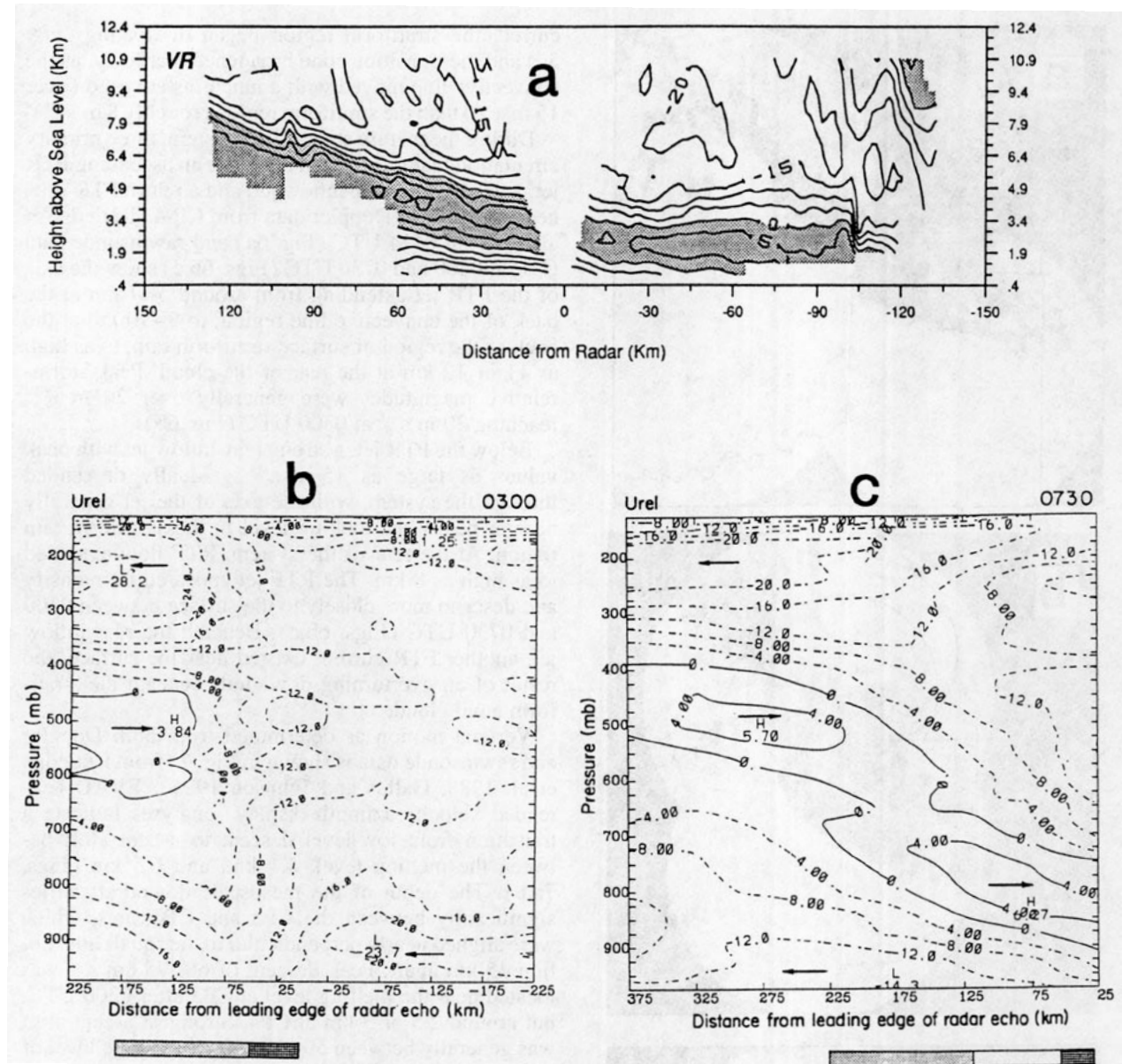


FIG. 6. Horizontal storm-relative velocities for the 11 June squall line from the (a) CP-4 Doppler radar at 0414 UTC (from Rutledge et al. 1988) and from the rawinsonde-based study of Gallus and Johnson (1991) at (b) 0300 and (c) 0730 UTC. Rawinsonde-derived values are taken from 3-hour composites centered at each time. Contour interval for the Doppler result is 5 m s^{-1} ; 4 m s^{-1} for the rawinsonde results. Shading in (a) represents rear to front flow. Bar below (b) and (c) represents position of the squall line with convective line darkest shading, stratiform region lighter shading, and transition zone between them.

around 30 cm s^{-1} . The strongest stratiform region ascent generally occurred around the 300-mb level or 9 km. This level is significantly lower than the majority of the peak levels diagnosed by the Doppler radars, but it agrees well with many other squall line cases (e.g., Gamache and Houze 1982). Doppler-derived vertical motions are susceptible to errors at high levels due to inaccuracies in the upper-boundary condition on w . Although aliasing of data also affects the diagnosed mesoscale downdraft, the rawinsonde data do indicate peak

descent of between 15 and 25 cm s^{-1} over broad regions, with the strongest descent near the same levels as found by the Doppler radars, generally near or just above the melting level. The rawinsonde data imply that the mesoscale downdraft may have extended to higher levels when the system was rapidly dissipating (Fig. 7e) and covered a region more than 200 km wide after 0600 UTC.

The 10–11 June system produced both surface pressure perturbations, including a surface mesohigh, pre-

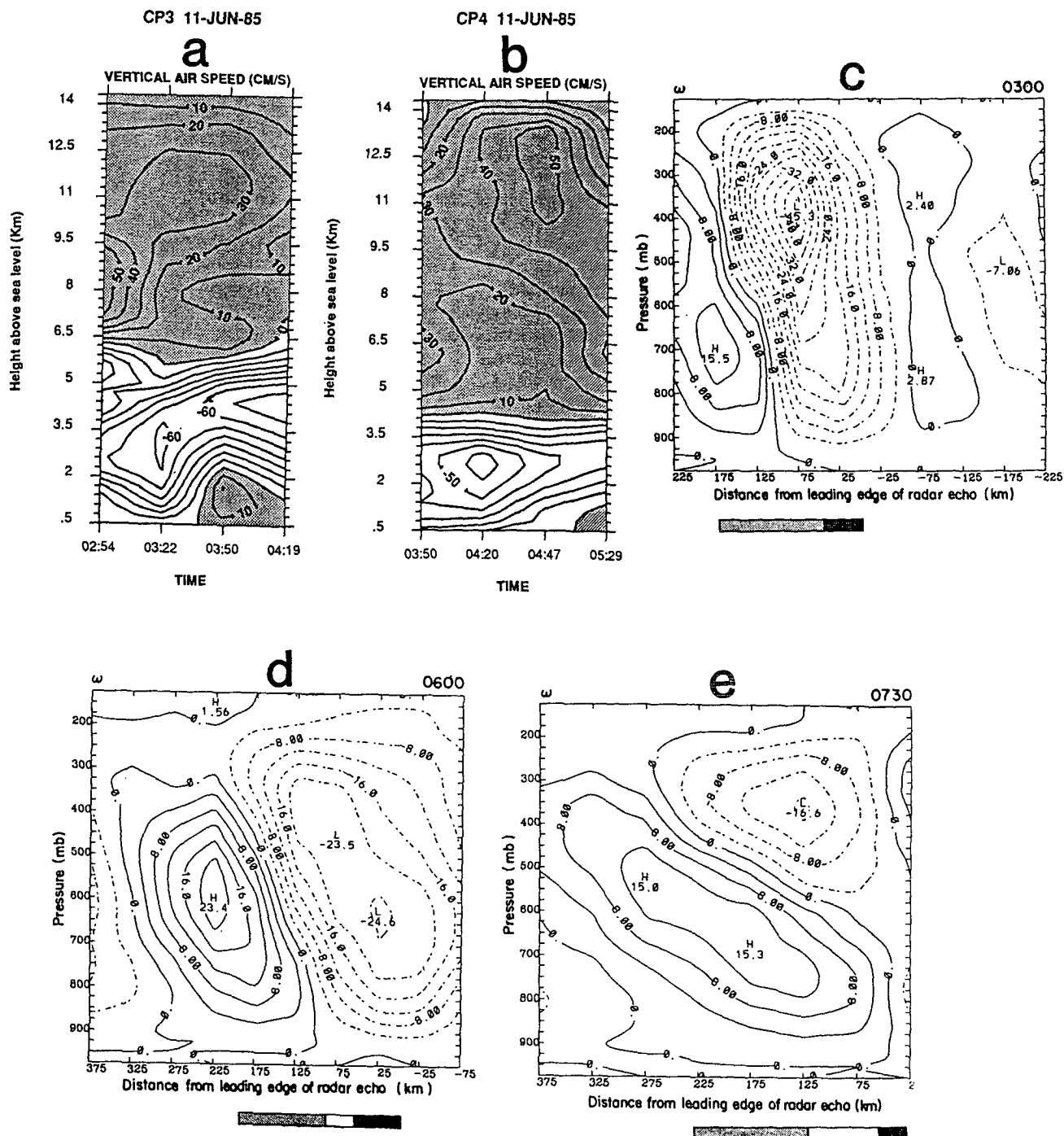


FIG. 7. Vertical velocity (w) for the 11 June system from EVAD Doppler analyses at (a) CP-3 between 0254 and 0419 UTC and (b) CP-4 between 0350 and 0529 UTC (from Rutledge et al. 1988), and (w) from kinematic method applied to rawinsonde data at (c) 0300, (d) 0600, and (e) 0730 UTC (from Gallus and Johnson 1991). Contour interval for Doppler data is 10 cm s^{-1} , and for rawinsonde data $4 \mu b s^{-1}$. Shading in (a) and (b) represents upward motion. Bar below (c), (d), and (e) is same as in Fig. 6. In (c)-(e), $1 \mu b s^{-1}$ is roughly 1 cm s^{-1} below 700 mb, roughly 2 cm s^{-1} at 400 mb, and 4 cm s^{-1} at 200 mb.

squall mesolow and wake low (Johnson and Hamilton 1988), and a midlevel mesolow (Gallus and Johnson 1992). The wake low just behind the back edge of sur-

face precipitation had local pressure perturbations as low as 2 mb below the region average around 0300 UTC, with about a 6-mb gradient over a 200-km dis-

tance between the wake low and the mesohigh centered at the back of the convective line region (Johnson and Hamilton 1988).

4. Simulation results

In the control simulation to be discussed in this paper (CTL), hydrometeors and heat advect into the domain in the pulsing manner discussed earlier. The amplitude of the pulses is modulated to represent the time variations observed in the convective line, with active convection and intense diabatic heating for approximately 3 hours, and a gradual weakening thereafter. The amplitude of the hydrometeor pulses decreases after 300 minutes, ceasing at 405 minutes. The amplitude of the convective heating pulses increases during the first 15 minutes, reaching a maximum that is maintained through 190 minutes. After this time, heating diminishes and is neglected after 300 minutes. Hydrometeors are assumed to be present in the dissipating convection, even during the time period when convective heating is becoming rather small.

a. Hydrometeor fields

In CTL, snow enters the domain and advects rearward, covering an area that expands with time (Figs. 8a,b). Snow quantities double from those present in the convective cores (Fig. 4) by 180 minutes (Fig. 8a). Most of the increase in snow mixing ratios, roughly 80%, is due to the autoconversion of ice to snow since ice mixing ratios exiting the convective line are significantly greater than the 0.4 g kg^{-1} conversion threshold used in the microphysical parameterization. Although vertical motions are weak in the domain through 180 minutes (to be shown later), slow fallspeeds ($1\text{--}1.5 \text{ m s}^{-1}$) allow vapor deposition to also add to the snow mass. Riming and collection of cloud ice play a less important role. As will be shown later, enhanced ascent occurs at the front of the anvil cloud, as has been observed by Doppler radar in this case (Matejka and Schurr 1991), and helps to increase vapor deposition onto snow that has entered the domain from the convective line. After 180 minutes broad areas of significant upward motion develop within the anvil cloud, increasing snow production. At 360 minutes (Fig. 8b), peak snow quantities reach 1.8 g kg^{-1} .

Low-density graupel, or more accurately aggregates of snow, also advect across the domain, but the peak quantities throughout the simulation are not significantly different from those entering the domain. Graupel does not grow by autoconversion from ice, as snow does. In addition, graupel falls slightly faster than snow, decreasing deposition and collection of ice. Significant amounts of graupel are generally restricted to within 100 km or so of the convective line at all times.

Large amounts of ice are converted to snow or collected by snow and graupel upon entering the domain

so that mixing ratios drop sharply near the right boundary (not shown). Significant ice is initiated in the layer 10–11 km after approximately 270 minutes, where vapor is present in sufficient quantities. Ice rapidly advects across the domain, reaching the rear boundary by 225 minutes.

Although cloud water advects into the domain from the convective line, it is quickly collected by snow and graupel, and sizeable amounts also evaporate in subsaturated air. Through the first 180 minutes of simulation, significant cloud water is restricted to points near the convective line. After this time, upward motion is stronger and small amounts of cloud water are present over a rather broad area by 360 minutes (Fig. 9). The peak quantities are only on the order of 0.1 g kg^{-1} . These small amounts of cloud water are supported by aircraft observations of lightly rimed aggregates in the stratiform region of the system (Willis and Heymsfield 1989).

Both snow and graupel fall through the melting level ($\sim 4.1 \text{ km}$), producing rain (Fig. 10). Rain reaches the surface shortly after 45 minutes and by 90 minutes covers a region 55 km wide with peak intensity of around 1.5 mm h^{-1} . At 180 minutes (Fig. 10a) rainfall expands to include all points within 80 km of the convective line. Rain quantities increase with time during the period that advection from the convective line occurs, and the peak amount, equivalent to a rain rate of 7 mm h^{-1} , occurs at 360 minutes (Fig. 10c), or an hour after convective heating has ceased and hydrometeor advection has significantly weakened.

The region experiencing surface rainfall in the model agrees reasonably well with the observed area, shown with a bar below each figure (Fig. 10). This agreement occurs at all times. After 270 minutes (Fig. 10b), a region with no appreciable rainfall widens just behind the convective line. This is also about the time that the weak echo (under 15 dBZ) region grew significantly in the observed system (see Fig. 5). This region, the transition zone, is primarily the result of fallspeed sorting in the model. At 315 minutes, rainfall covered the region 25–110 km behind the convective line. This region shifted to $x = 45\text{--}145 \text{ km}$ at 360 minutes (Fig. 10c) and 90–180 km behind at 405 minutes. At nearly all times, the model surface rainfall region is within 10–20 km of the observed region. The location of peak observed surface rainfall is shown with darker stippling in Fig. 10. The model again reproduces the rearward shift with time of the heaviest surface rainfall. The rearward shift is due both to the increasing strength of FTR flow transporting hydrometeors rearward and to the development of ascent within the anvil.

In situ production of condensate becomes increasingly important after 270 minutes in the model simulation. In fact, peak rain mixing ratios, peak surface rainfall rates, and areal coverage of rain all occur during the hour after hydrometeor advection from the convective line has peaked. At the end of the simulation,

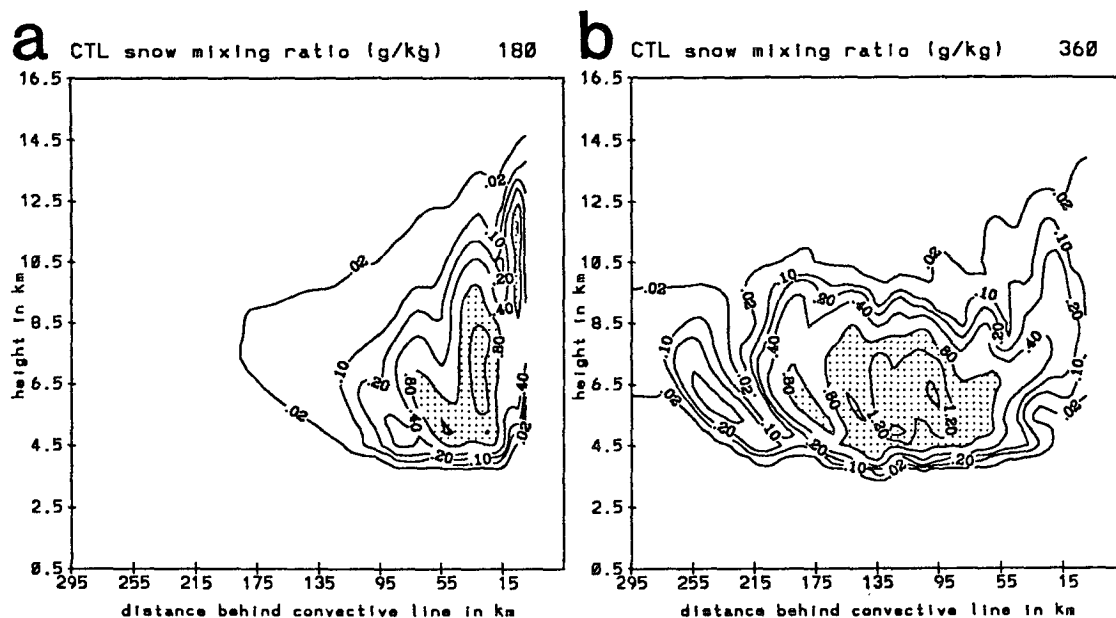


FIG. 8. Mixing ratios (g kg^{-1}) in the control model simulation of snow at (a) 180 and (b) 360 minutes. Contours at 0.02, 0.1, 0.2, 0.4, 0.8, 1.2, and 1.6 g kg^{-1} , with values above 0.8 g kg^{-1} shaded.

405 minutes, the complete absence of hydrometeor advection from the convective line does result in diminishing rainfall rates and a smaller area of surface rainfall. In general, the model produces the heaviest rain at the surface during the 315–360-min period, when rates reach 3.4 mm h^{-1} . In a broad sense, the timing of the heaviest rainfall agrees reasonably well with precipi-

tation observations (Rutledge and MacGorman 1988) and radar reflectivity measurements, which indicated the highest reflectivities in the stratiform region occurred between 0430 and 0530 UTC. However, PAM and SAM mesonetwork rain gauges showed that peak rain rates in the stratiform region were around 6 mm h^{-1} (GJ). As will be shown later, the failure of the model to accurately diagnose the intensity of the surface rainfall is at least partially due to the weakness of upward motions simulated at high levels in the anvil cloud. Average rainfall rates at the surface remained rather close to 1 mm h^{-1} throughout the simulation. GJ found average stratiform rain rates to generally lie between 2 and 3.3 mm h^{-1} . Therefore, the model values again were roughly one-half of the observed.

The transition zone is simulated well with the model, broadening most rapidly late in the simulation. Observations showed the greatest broadening after 0600 UTC. A simulation like CTL but without dissipation of the convective line resulted in a less pronounced transition zone that was not nearly as broad. Although a region of generally lighter surface rainfall did occur behind the convective line, meeting the definition of transition zone, rain rates of over 0.5 mm h^{-1} were common there until 405 minutes. Rainfall immediately behind the convective line did not change appreciably over time. This indicates that the rapid growth of a transition zone with almost no rainfall late in the lifetime of the 10–11 June system was primarily due to the rapid dissipation of the convective elements. Although fallspeed sorting and enhanced subsidence behind the convective line can result in the formation of

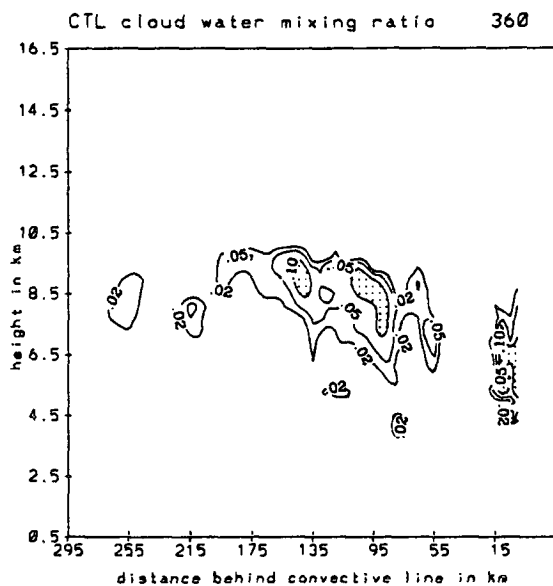


FIG. 9. Mixing ratios (g kg^{-1}) of cloud water at 360 minutes. Contours at 0.02, 0.05, and 0.1 g kg^{-1} , with values above 0.1 g kg^{-1} shaded.

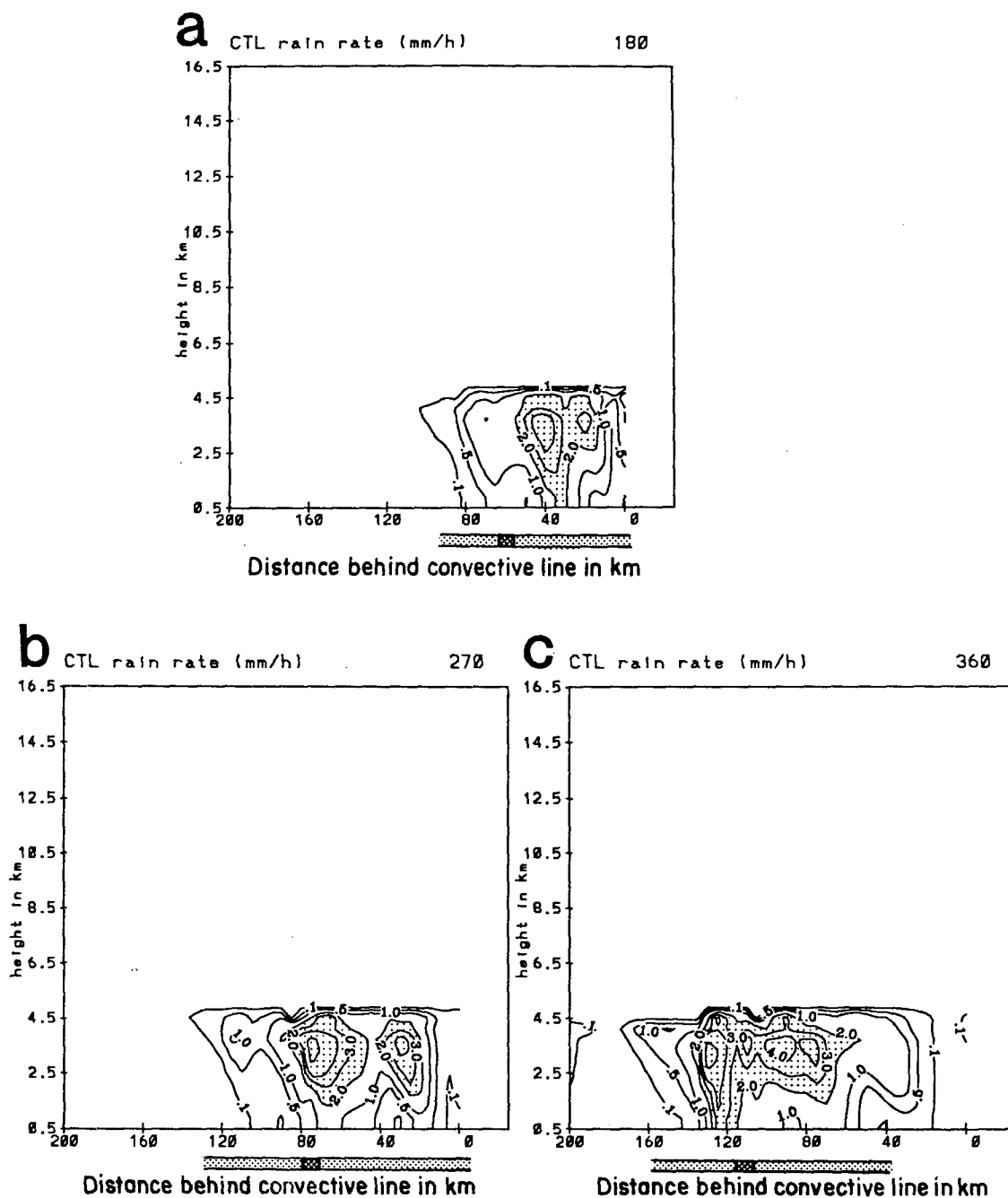


FIG. 10. Rain rates (in mm h^{-1}) for (a) 180, (b) 270, and (c) 360 minutes of model simulation. Contours at 0.1, 0.5, 1, 2, 3, 4, 6, and 8 mm h^{-1} , with values above 2 mm h^{-1} shaded. Rightmost 200 km of the domain is shown in each figure. The area of observed rain is shown with a bar below each figure. Enhanced rainfall is shown with darker stippling.

a transition zone, the total lack of rain over a broad region may require the rapid dissipation of the convective line.

b. Vertical motion

Vertical motions develop within the domain (Fig. 11) that are qualitatively similar to observations (Fig.

7). As in the modeling work of Lafore and Moncrieff (1989), large amplitude gravity waves exist in the stratiform region, so to better represent meaningful circulations the fields of vertical velocity and horizontal wind were averaged over 20-min periods centered at given times. This time period is far shorter than that used in Lafore and Moncrieff, and no horizontal aver-

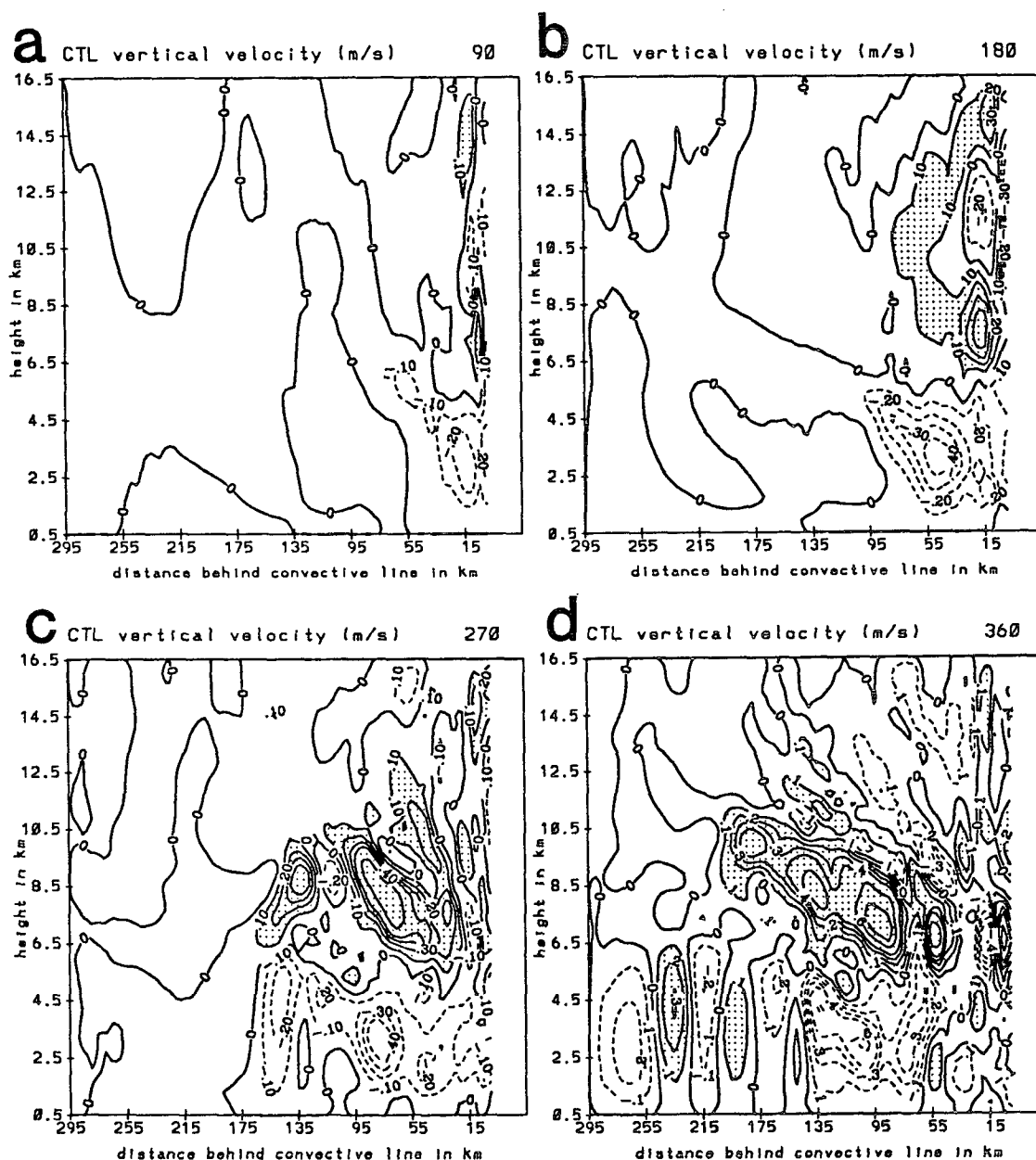


FIG. 11. Vertical velocities in the model domain at (a) 90, (b) 180, (c) 270, and (d) 360 minutes. For absolute values within 0.4 m s^{-1} , contour interval is 0.1 m s^{-1} , with an interval of 0.2 m s^{-1} for greater values. Ascent greater than 0.1 m s^{-1} is shaded.

aging was performed. This minimal amount of smoothing is generally sufficient to reveal the important circulations. The advection of hydrometeors, the resultant melting into rain, and evaporation of the rain rapidly produce a fairly well-developed mesoscale downdraft, which can be clearly seen at 90 minutes (Fig. 11a). Peak descent is nearly 30 cm s^{-1} at the 2.9-km level. Significant descent occurs over a region nearly 50 km wide and extends farther rearward in a band near and just above the melting level (4.1 km), reaching up to over 7 km about 90 km rearward from the convective

line. This band of descent is the result of sublimational cooling in this region (figure shown later).

The mesoscale downdraft broadens and intensifies through 270 minutes (Figs. 11b,c) with peak descent reaching over 50 cm s^{-1} . The most intense downward motion continues to move rearward relative to the convective line. Most of the downward motion is restricted to below the melting level, although there is a tendency for downward motion to exist at higher levels to the rear of the surface rainfall. At 360 minutes (Fig. 11d), the strongest descent, over 60 cm s^{-1} , is roughly 100

km rearward from the convective line region. Significant downward motion covers a region 110 km wide. The multiple peaks in both descent and ascent at later times (Figs. 11c,d) are only partially due to the pulsing of the convection. A sensitivity test without pulsing (not shown) found that similar peaks develop, but with less magnitude.

The mesoscale downdraft in the model (Fig. 11) agrees reasonably well with observations (Fig. 7). For instance, GJ found mesoscale descent over a roughly 150-km region at 0600 and 0730 UTC. At approximately the same time, the model diagnoses 10 cm s^{-1} or greater descent over a 100 km or greater area.

The mesoscale updraft within the anvil cloud is known to be important in explaining the surface rainfall rates observed within the stratiform region. In several simulations of squall lines, models have failed to adequately diagnose updrafts as intense as those derived from Doppler radar or rawinsonde data (e.g., Dudhia et al. 1987). The same problem occurs to some degree in this simulation. At 90 minutes, there is no broad region of ascent within the domain (Fig. 11a). Weak ascent (under 5 cm s^{-1}) occurs above the mesoscale downdraft except in a narrow band just behind the buffer zone where saturated conditions allow significant condensation and vapor deposition to take place.

By 180 minutes (Fig. 11b), a more pronounced mesoscale updraft forms in the domain. Upward motions reach 10 cm s^{-1} within a region roughly 75 km wide. A narrow band of much stronger ascent, nearly 50 cm s^{-1} , can be found within 20 km of the convective line. This location would actually be in the region of the transition zone in the 10–11 June squall line and would be similar to squall line cases studied by Smull and Houze (1987a) and Chong et al. (1987). Tao and Simpson (1989) found in a GATE case that most of the deposition and condensation was occurring within the front 40–50 km of a stratiform region. This would agree with these results during the first 180 minutes of the simulation, where the strong ascent is restricted to just behind the convective line.

At 270 minutes (Fig. 11c), a very broad mesoscale updraft covers much of the model domain, and sizeable regions experience ascent exceeding 20 cm s^{-1} . Peak values exceed 70 cm s^{-1} around the 7.5-km level. The strongest ascent is concentrated in a layer roughly 4 km deep between 6.5 and 10.5 km, with some hint that updraft maxima sloped rearward with height. Although the upward motions are significant, they are somewhat less intense over broad regions than those measured by Doppler radar for this case. Rutledge et al. (1988) diagnosed upward motions over broad regions between 30 and 60 cm s^{-1} within the anvil cloud. That same study found that the peak ascent occurred at a rather high level, 11–12 km. This level would be several kilometers higher than the peak level diagnosed by the model, but the Doppler results may be in error near cloud top (Srivastava et al. 1986). The rawinsonde

study of GJ for this case, along with observational studies of other squall lines (e.g., Ogura and Liou 1980; Chong et al. 1987) and other numerical simulations (Zhang et al. 1989), generally found a somewhat lower level of peak ascent, agreeing more with the results of this simulation. The peak ascent found in this simulation at 270 minutes agrees with the peak value obtained in the 3D simulation of this case by Zhang et al. (1989). In both cases, however, such intense upward motion was restricted to rather small areas.

At 360 minutes (Fig. 11d), significant ascent occurs over a region 170 km wide from $x = 40$ to 210 km, with peak values of nearly 1 m s^{-1} around the 7-km level. At this time, both the scale and magnitude of upward vertical motion agree best with observations (Figs. 7b, d, e). After this time, upward motions, though still strong in places, are generally weakening, and the mesoscale updraft is becoming more disorganized.

From Fig. 12, it can be seen that the model diagnosed vertical motion averaged over the entire stratiform rain region during the 270–360-min time period agrees qualitatively with the rawinsonde diagnosed values averaged at 0600 and 0730 UTC from GJ. The model values averaged over a smaller 40-km region near the heaviest stratiform rainfall compare well at low levels with an average of the CP3 and CP4 EVAD analyses

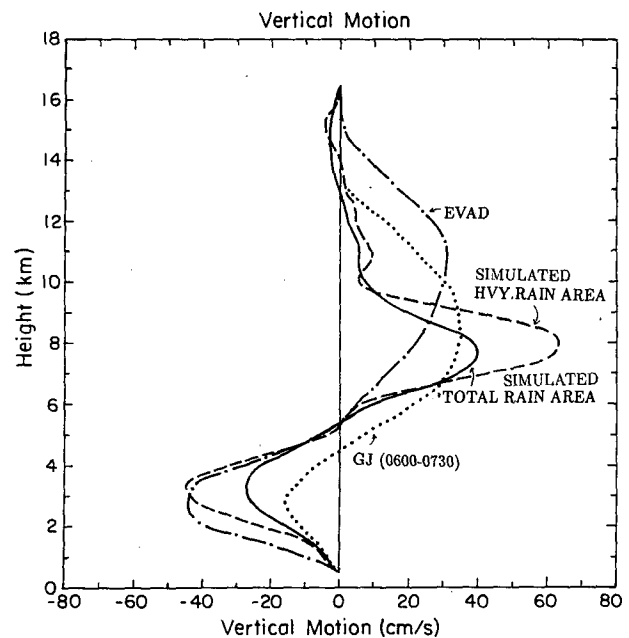


FIG. 12. Vertical motion averaged over the stratiform rain region in the model during the 270–360-min time period (solid curve) compared with rawinsonde-derived average over the same region at 0600 and 0730 UTC (dotted curve, from Gallus and Johnson 1991). Model averaged vertical motion over 40-km region of heaviest stratiform rainfall during the 270–360-min period (dashed curve) is compared with similar areal average from EVAD analyses of Doppler data (dashed-dotted curve, from Rutledge et al. 1988).

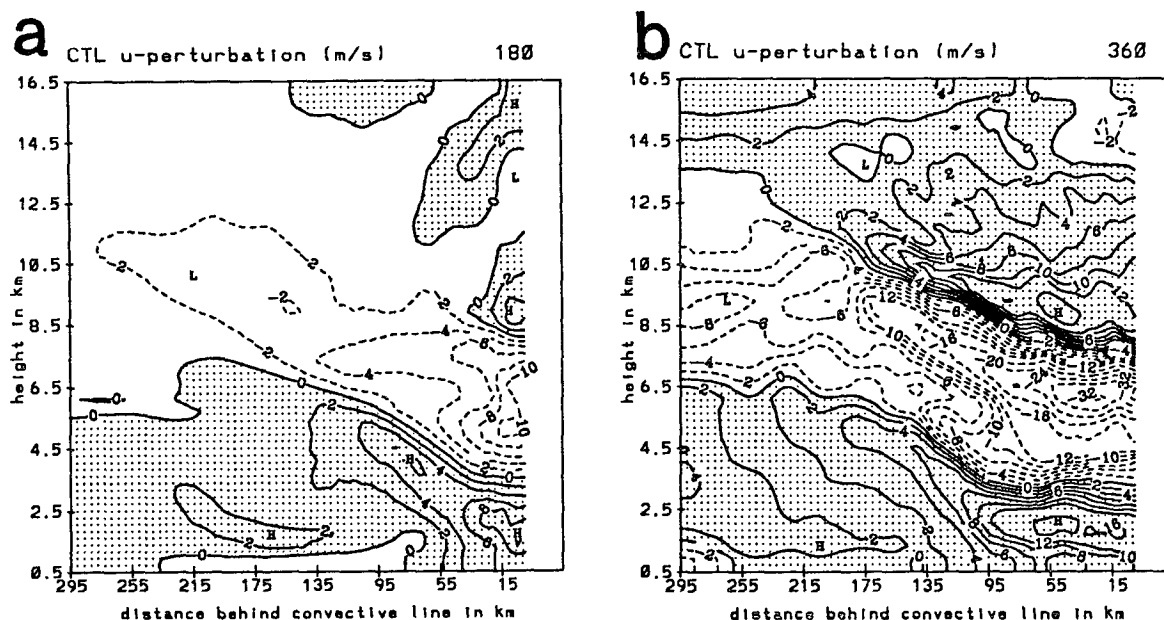


FIG. 13. Perturbation u velocities at (a) 180 and (b) 360 minutes. Front-to-rear flow is dashed, and rear-to-front flow is shaded. Contour interval of 2 m s^{-1} for absolute values less than 12 m s^{-1} , with an interval of 4 m s^{-1} for greater values.

around 0400 UTC (Rutledge et al. 1988), which each represented a region 40 km in diameter. Over the entire region experiencing stratiform rain, the model indicates roughly $5\text{--}10 \text{ cm s}^{-1}$ more low-level subsidence than found by rawinsondes. The difference may be due to the failure of the rawinsonde study to fully resolve the downdraft. Regionwide ascent peaks at nearly 40 cm s^{-1} , in good agreement with the ascent diagnosed from rawinsondes. However, the peak upward motion in the model is considerably lower than the EVAD peak and about 1 km lower than the rawinsonde-derived value.

The model and EVAD results for the mesoscale downdraft agree very well. All four curves show peak descent not far from the 3-km level. The crossover from downward to upward motion in the model occurs near 5 km, in excellent agreement with the EVAD curve. Upward motion in this 40-km region is as large as 65 cm s^{-1} at 8.0 km. This exceeds the peak value of the averaged EVAD curve but is similar to some measurements made at the CP3 and CP4 radars at specific times. Again, however, the model finds upward motion restricted to a relatively shallow region with upward motions above 9 km underestimated. This underestimate at high elevations may be partly due to the omission of radiative effects in the model. Weak subsidence at or above the cloud top in both the model EVAD-scale profile and the systemwide average is supported by observations from the stratiform region of this case (Johnson et al. 1990).

c. Horizontal circulations

Almost immediately, heating and cooling associated with microphysical processes within the domain induce

a perturbation horizontal RTF flow below 6 km with the strongest RTF perturbation flow just behind the convective line in a steeply sloped zone (Fig. 13). The RTF flow first develops just behind the convective line but expands to cover a 100-km region at 180 minutes (Fig. 13a). These findings resemble the dual-Doppler observations of a North Dakota squall line by Klimowski (1994). The intensity increases from 3 m s^{-1} at 90 minutes to 10 m s^{-1} at 180 minutes. Similarly, FTR flow is enhanced generally in the 4–8-km layer behind the convective line with magnitudes reaching 10 m s^{-1} . The perturbations intensify throughout the simulation with the strongest perturbations, around 17 m s^{-1} , occurring after the advection has ceased from the convective line at 360 minutes (Fig. 13b). This rear-inflow “jet” becomes increasingly horizontal over time, much the same as the observed jet for this case (e.g., GJ). Early in the simulation, weak FTR perturbation flow occurs beneath the rear-inflow jet at the surface as the cold pool from the convection and growing stratiform rain region spreads rearward. The FTR perturbation flow aloft also intensifies through 360 minutes and is concentrated in a band that slopes upward toward the rear. At the later times, generally after 180 minutes, a return branch of RTF perturbation velocity exists around the 9- or 10-km level.

The total storm-relative wind is shown in Fig. 14. At 90 minutes (not shown), the total flow is primarily from FTR, with weak RTF flow in the front portion of the domain. The rear-inflow jet strengthens, with the peak velocities reaching 14 m s^{-1} by 360 minutes (Fig. 14b). The FTR flow increases to over 30 m s^{-1} . These diagnosed values of FTR flow, although quite strong, are

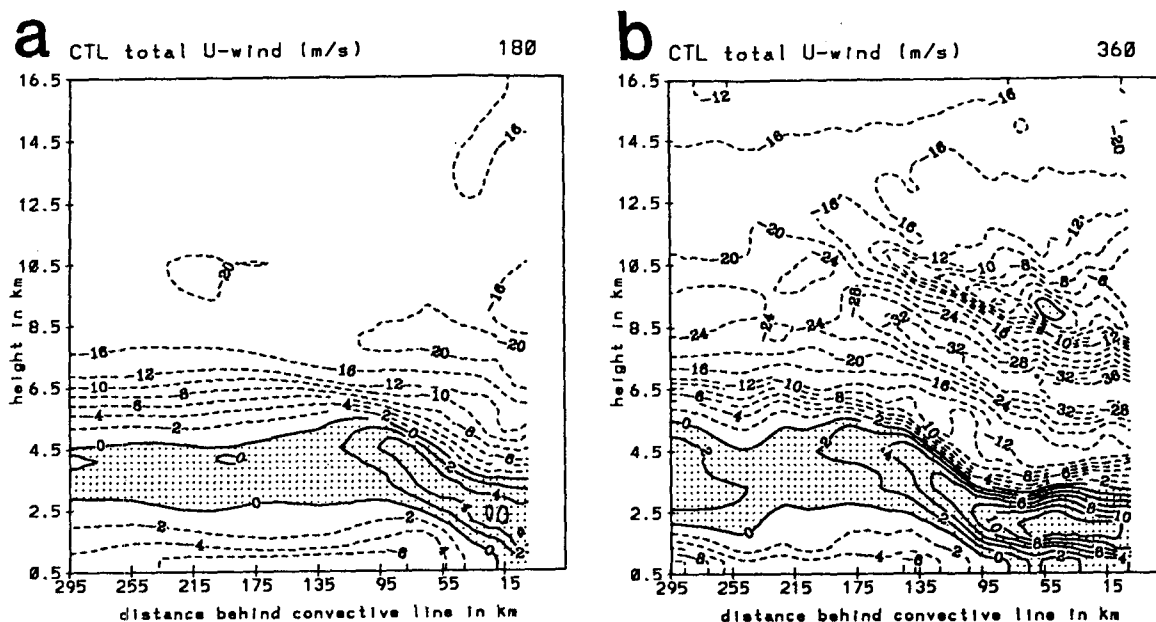


FIG. 14. Same as Fig. 13 except for total storm-relative u velocity (includes ambient flow).

only slightly larger than the peak values found by the Doppler and rawinsonde observations from this case (Smull and Houze 1987b; Rutledge et al. 1988; Gallus and Johnson 1991). The diagnosed rear-inflow jet, however, is weaker than observed. Rutledge et al. (1988) found that RTF flow exceeded 15 m s^{-1} by 0300 UTC. Rawinsondes also showed isolated values of 15 m s^{-1} , generally after 0300 UTC. It is believed that the model's

underestimate of upward motion in the anvil cloud and subsequent failure to produce enough precipitation led to underestimates of evaporation and sublimation, and the underestimated cooling may have prevented the rear-inflow current from strengthening to observed values. The model results also imply, however, that the system itself only generates strong rear-inflow within several hundred kilometers of the system. Even by the end of

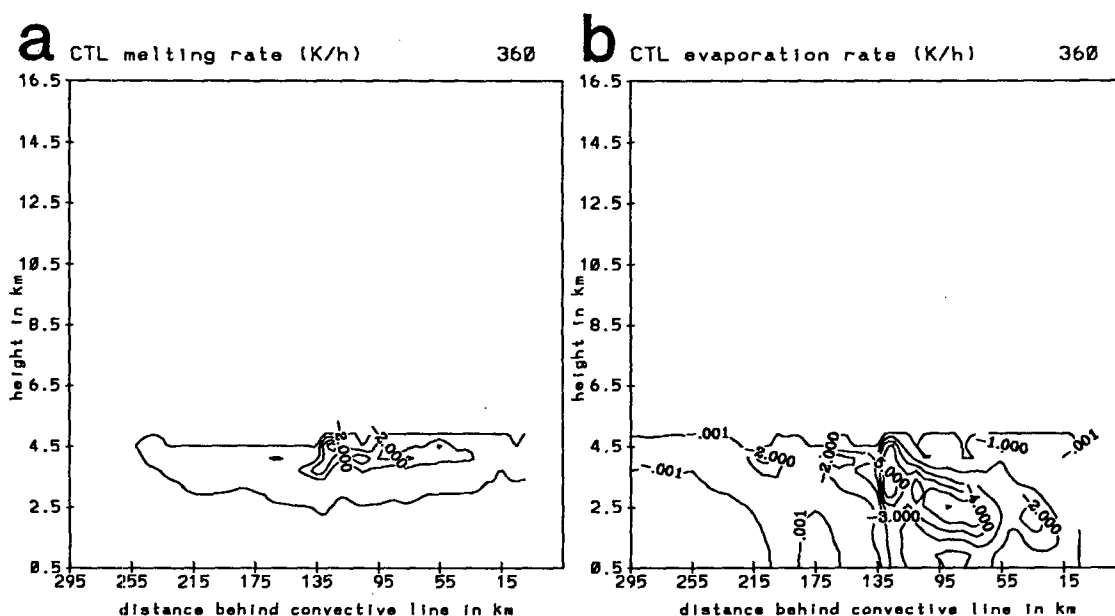


FIG. 15. Cooling rates from (a) melting and (b) evaporation at 360 minutes. Contour interval is 1 K h^{-1} .

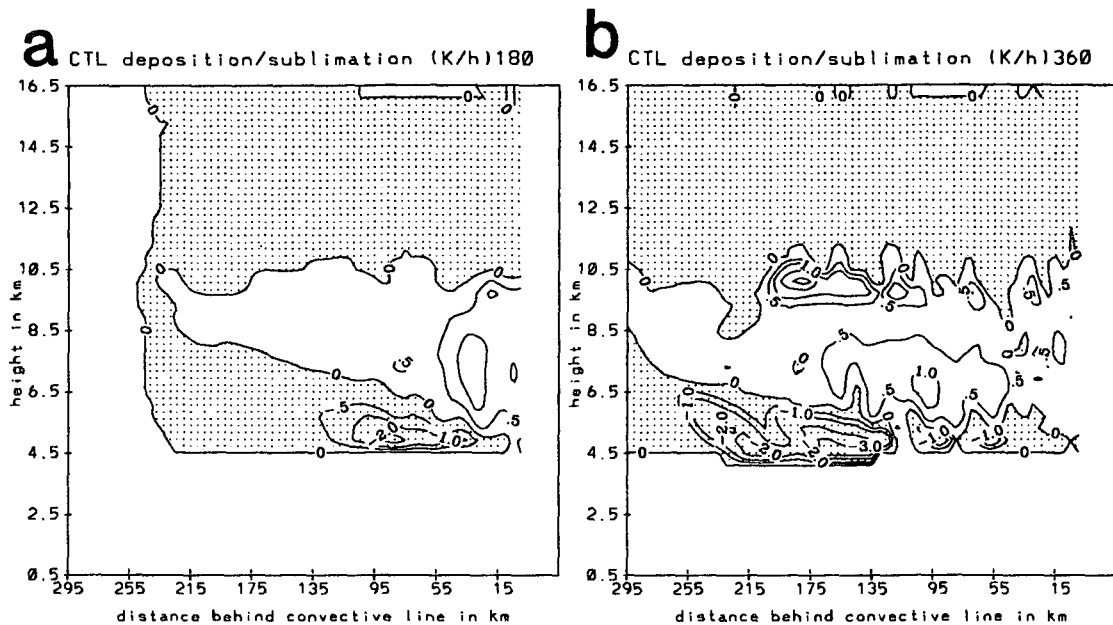


FIG. 16. Heating and cooling rates from deposition and sublimation at (a) 180 and (b) 360 minutes. Cooling is shaded. Contour interval of 0.5 K h^{-1} is used for absolute values less than 1 K h^{-1} , with an interval of 1 K h^{-1} for greater values.

the simulation, most of the significant rear-inflow was occurring within 150 km of the back of the convective line. The results of Rutledge et al. (1988) and GJ for this case show strong rear inflow well to the rear of this point. The numerical simulations of Zhang et al. (1989) were able to produce significant rear inflow many hundreds of kilometers to the rear of the system, which they attributed to large-scale baroclinicity. The failure of this simulation, along with many others using different initial conditions, to produce rear-inflow greater than 10 m s^{-1} well behind the system implies that large-scale baroclinicity may indeed be the mechanism responsible for the strong elevated portion of the jet on 10–11 June.

d. Microphysical processes

Melting in the simulation is restricted to a layer roughly 1 km deep near 4 km, with peak cooling rates just under 3°C h^{-1} through 270 minutes and approaching 4°C h^{-1} at the time of heaviest rainfall, 360 minutes (Fig. 15a). These cooling rates lie within the $1\text{--}6^\circ \text{C h}^{-1}$ range given by Leary and Houze (1979) for stratiform regions of MCSs (Fig. 15a) and are in reasonable agreement with the $2.5\text{--}2.9^\circ \text{C h}^{-1}$ rates inferred for this case by Willis and Heymsfield (1989).

Evaporative cooling occurs over a large area that expands rearward with time, covering a roughly 200 km area at 360 minutes (Fig. 15b). These cooling rates generally exceed those of both melting-induced cooling and sublimative cooling (to be shown later), with peak values in the region of heaviest precipitation between 5 and 7°C h^{-1} (Fig. 15b) at most times. Significant

evaporative cooling occurs over a much broader and deeper region than melting. The most intense cooling lies in a band that slopes rearward with height. This band is associated with the dry rear-inflow that develops.

Sublimation results in significant cooling over a larger region than melting, but over a slightly less area than evaporation (Fig. 16). The greatest cooling occurs just above the melting level where significant amounts of snow and graupel are present in the area where the rear-inflow jet is advecting dry air. Peak cooling rates exceed 2°C h^{-1} at 180 min (Fig. 16a) and 3°C h^{-1} at 360 min (Fig. 16b), values comparable to those of melting. Depositional heating occupies a broad region, but the heating is generally under $0.5^\circ \text{C h}^{-1}$. The most intense depositional heating occurs in regions of strong updraft and water supersaturation that also tend to have substantial condensational heating (Fig. 17). Peak depositional heating rates generally do not exceed $2.0^\circ \text{C h}^{-1}$. This differs from condensational heating, which already has a peak of over 4°C h^{-1} by 180 minutes (Fig. 17a) and nearly 10°C h^{-1} by 360 minutes (Fig. 17b). However, significant condensational heating is restricted to rather small regions within the anvil cloud, especially at early times.

A water budget of the domain shows that in situ production of condensate through deposition and condensation becomes increasingly important with time (Fig. 18). The water budget terms are expressed as percentages of the condensate mass being made available in the domain at each time. During roughly the first third of the model simulation, over 85% of the condensate being made avail-

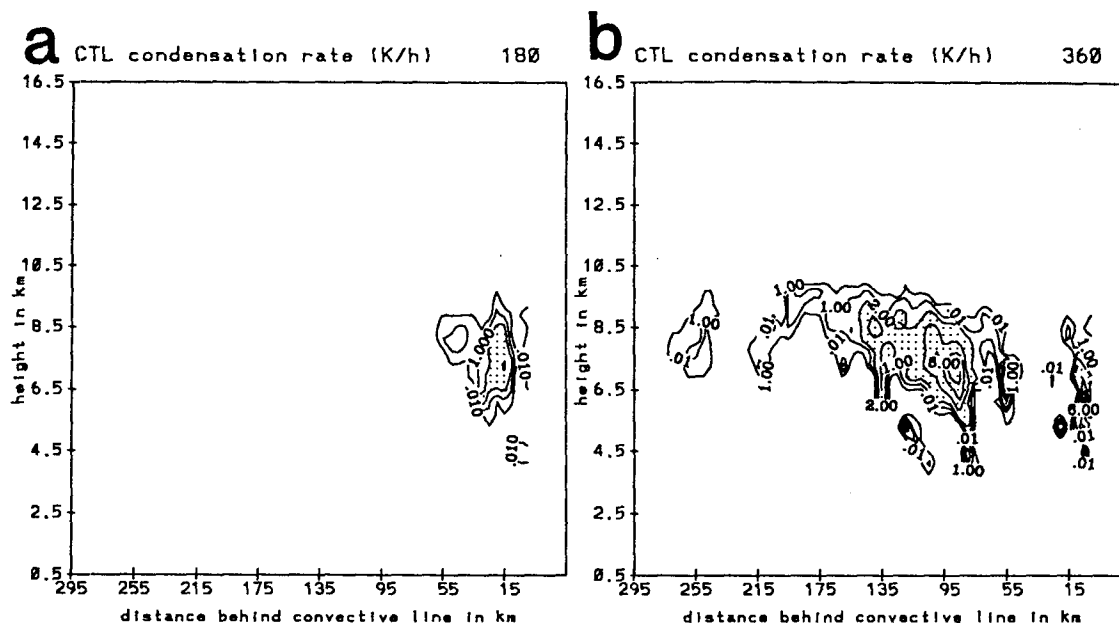


FIG. 17. Condensational heating rate at (a) 180 and (b) 360 minutes. Smallest contour is for 0.1 K h^{-1} , with other contours at 1, 2, 4, 6, 8, and 10 K h^{-1} . Heating greater than 2 K h^{-1} is shaded.

able in the domain is advected there from the convective line. Only 15% of the condensate is produced in situ with deposition supplying over twice as much condensate as

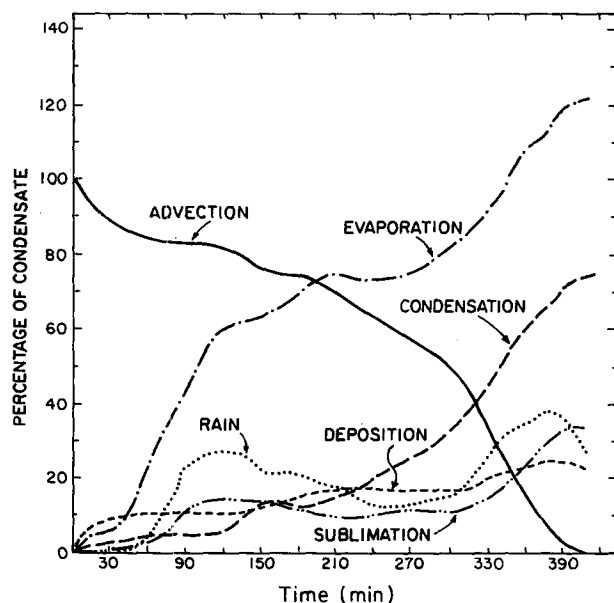


FIG. 18. Water budget of the control model simulation expressed in percentage of total condensate mass made available at each time. The 30-min running averages are used to remove effects of pulsing. Shown are advection from the convective line (solid line), condensation (long-dashed line), deposition (short-dashed line), evaporation (dashed-dotted line), sublimation (dashed-double dotted line), and rain (dotted line).

condensation. Condensation contributes more mass than deposition by 240 minutes, and the total in situ production increases to an average of 33% during the 135–270-min time period. By the period of heaviest stratiform rainfall, the last third of the simulation, 67% of the condensate made available in the domain is produced in situ, with nearly 75% of that total from condensation. Tao et al. (1993) also found in a numerical simulation of this case that advection of hydrometeors from the convective line supplied nearly all of the condensate in the stratiform region during the initial stage of the system, but less than half during the mature stage. For the entire 405 minutes of the present simulation, condensate advected from the convective line in this model supplied 55.8% of the total condensate available within the domain. This agrees almost exactly with the 56% figure given in Tao et al. (1993) over the course of their 16-hour simulation.

Gamache and Houze (1983) found that 25%–40% of the surface rainfall in the stratiform region of a tropical squall line was due to in situ production. GJ estimated roughly equal contributions from advection and in situ production during the later stages of the 10–11 June squall line. The kinematic model used by Rutledge and Houze (1987) determined that as much as 80% of the stratiform rainfall was due to in situ condensate production. Precipitation efficiencies, expressed as the percent of condensate being made available that falls out as precipitation at the surface at any time, are low throughout the simulation, generally 15%–20%. Late in the simulation, the efficiencies increase to over 30%. Evaporation is by far the largest sink term in the water budget, with an average of 76% of the available condensate lost during

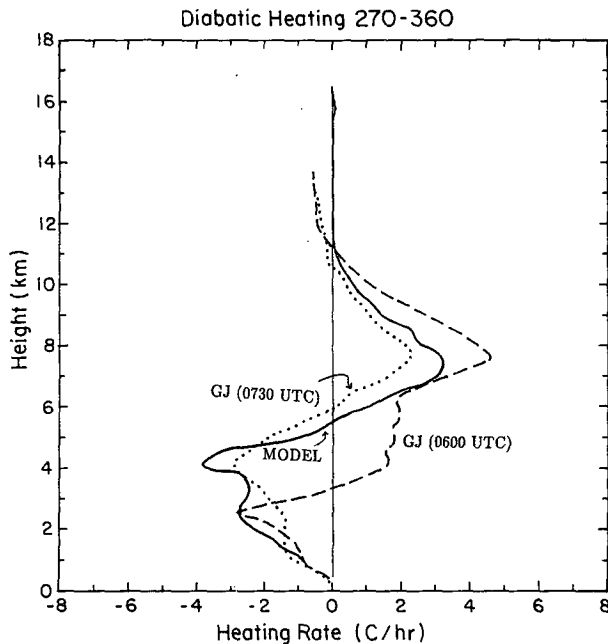


FIG. 19. Diabatic heating averaged over the region of surface stratiform rainfall during the 270–360-min time period in the model. Solid curve represents the model heating. Dashed curve is taken from the Q_1 budget of Gallus and Johnson for this case, valid at 0600 UTC, and dotted curve is from the budget at 0730 UTC.

the middle third of the simulation and 87% lost during the final third. Sublimation removes much less condensate, and the rates are similar to the creation rates by deposition.

Averaged diabatic heating within the entire stratiform rain region during the 270–360-min time period agrees reasonably well with Q_1 , the apparent heat source computed by GJ for the mature and dissipating stages of the system (Fig. 19). The model appears to simulate the diabatic cooling at low levels realistically, with cooling rates generally slightly larger than observed by the rawinsonde-based budget study. The shape of the curve is very similar to that of the 0730 UTC observation. The rather low crossover from cooling to warming indicated on the 0600 UTC curve is most likely the result of aliasing of convective heating into the region of stratiform cooling. Aliasing of data was more pronounced at this time than at 0730 UTC since the transition zone was narrower. The model indicates two peaks in the cooling, consistent with the results of Houze (1982). The lower cooling peak is found at around 2.5 km, and the higher one at the melting level. A similar two-peaked structure of the microphysical cooling was found by Chong and Hauser (1990) in the stratiform region of a COPT tropical squall line.

Model estimates of peak heating around 3.5 K h^{-1} at the 400-mb level agree reasonably well with the rawinsonde-derived curves. The peak heating rate falls between the values at 0600 and 0730 UTC. Because the 0730 UTC profile is representative of a dissipating

stratiform region, the simulated profile should be closer to the 0600 UTC curve. However, aliasing may have artificially increased the values at 0600 UTC. In any case, it appears the model is underestimating diabatic heating by approximately 20%, with the primary underestimation occurring at higher levels in the anvil cloud. This slight underestimate may partially explain the lighter than observed surface rainfall in the model. The diminished diabatic heating is associated with the relatively weak ascent at high levels (Fig. 12).

The individual contributions to the diabatic heating at 315 minutes averaged over the stratiform region are shown in Fig. 20. The lower diabatic cooling peak is due entirely to evaporation of rain, while the peak near the melting level is a function of evaporation, sublimation, and melting. The total cooling due to both sublimation and melting are somewhat similar, with each acting in a relatively narrow layer. It can be seen in the figure that diabatic heating in the anvil cloud is due primarily to condensation at this time, although vapor deposition is contributing somewhat uniformly just under 1 K h^{-1} through the layer 6–10 km. Although condensational heating is more intense, depositional heating is significant and releases heat higher in the anvil cloud than does condensation. As implied in Figs. 16, 17, and 18, at earlier times condensation rates were relatively smaller.

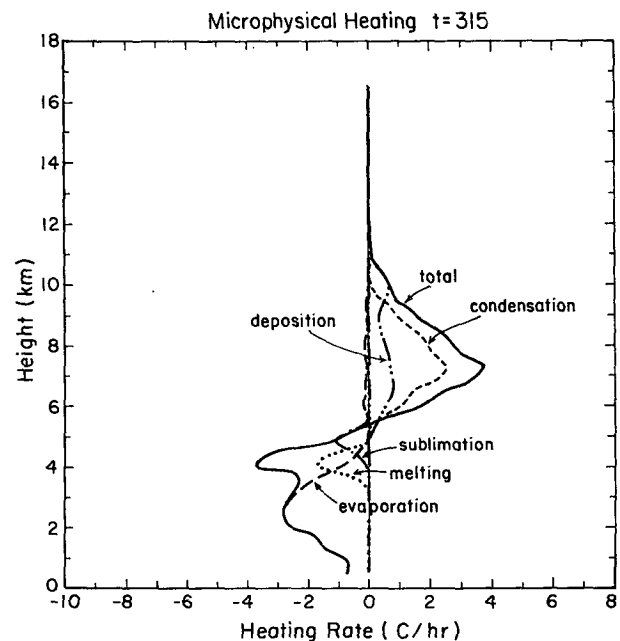


FIG. 20. Individual microphysical heating and cooling rates at 315 minutes, averaged over the region of surface stratiform rain. Total heating or cooling: solid line, cooling from evaporation: long-dashed, sublimation: dash-dotted, depositional heating: dash-double dotted, cooling from melting: dotted, and condensational heating: short dashed.

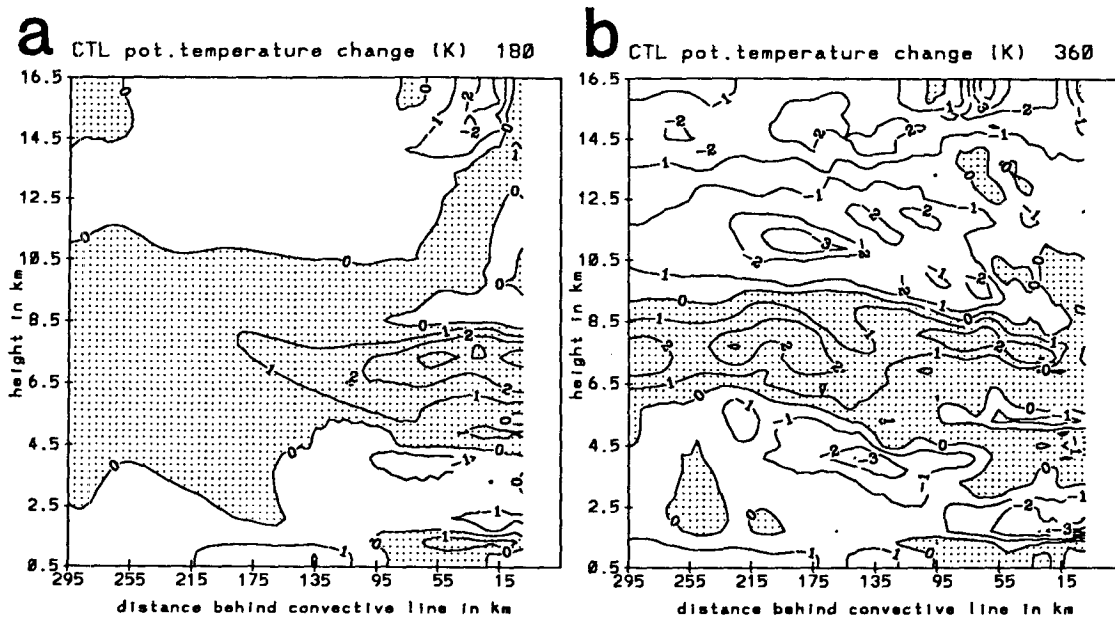


FIG. 21. Potential temperature change since start of model simulation at (a) 180 and (b) 360 minutes. Contour interval is 1 K; warming is shaded.

e. Temperature and pressure changes

The effect of the diabatic heating, along with adiabatic temperature changes from the vertical motions occurring in the domain, can be seen in the field of perturbation potential temperature (Fig. 21). The neg-

ative perturbations at 180 minutes (Fig. 21a) are greatest in two separate regions; one at lower levels around $x = 15$ km due to evaporation, and another farther rearward caused by both melting and evaporation. Some of the evaporative cooling at low levels is opposed by strong adiabatic warming from the mesoscale down-

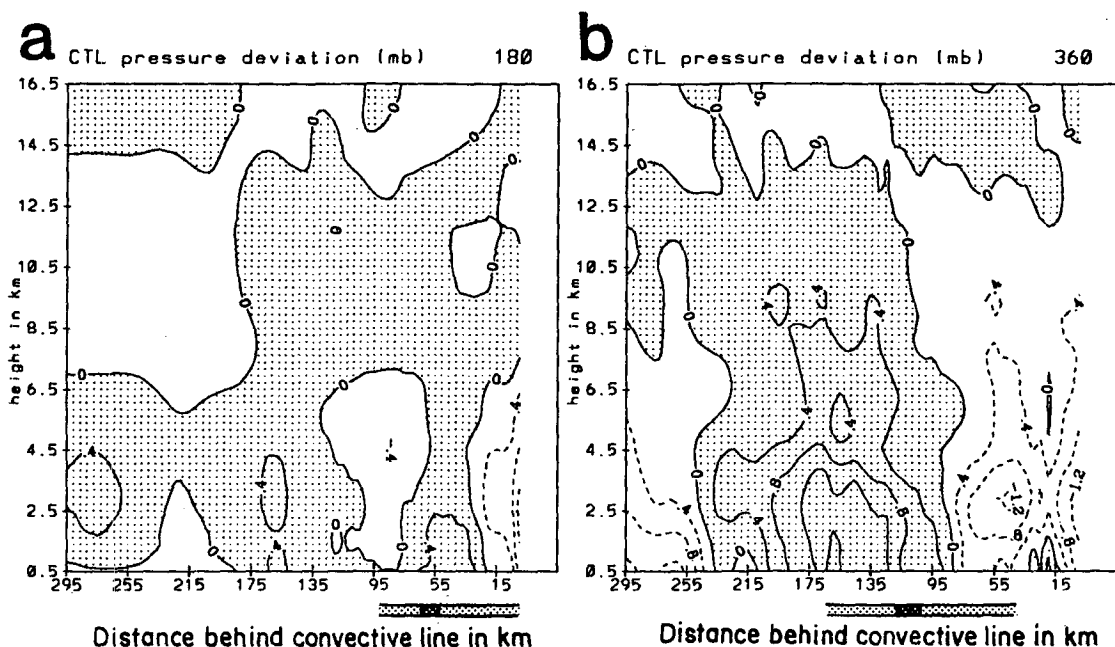


FIG. 22. Hydrostatically derived pressure deviation from domain average at (a) 180 and (b) 360 minutes. Contour interval is 0.4 mb. Positive values shaded; negative values are dashed. Region of simulated surface rainfall shown with a bar below each panel; heavier rainfall in darker stippling.

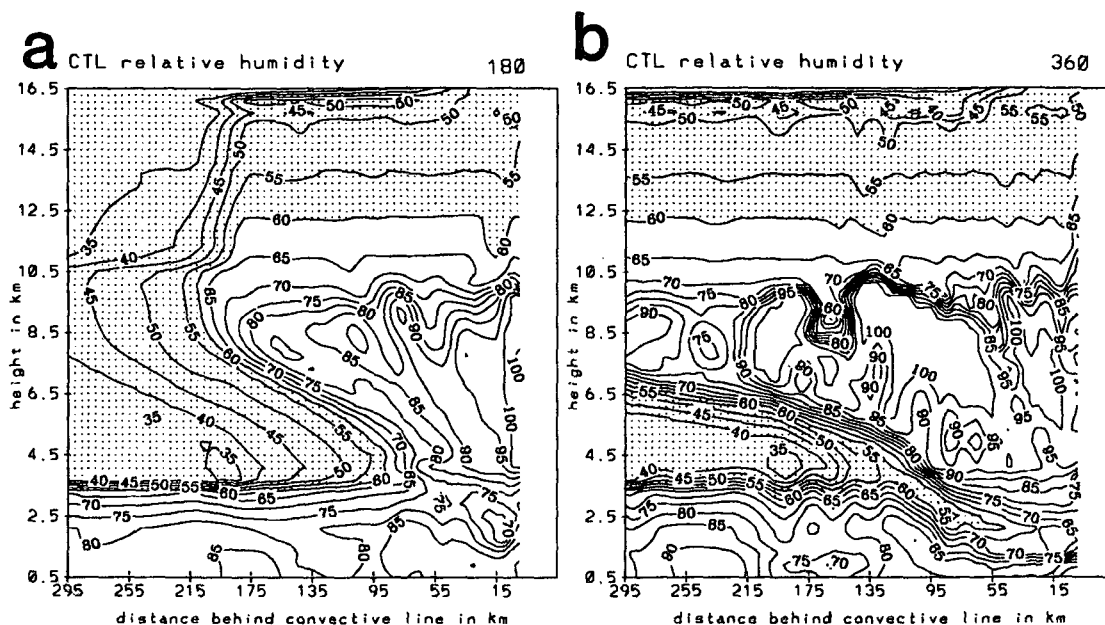


FIG. 23. Relative humidity with respect to water at (a) 180 and (b) 360 minutes. Contour interval 5%. Humidities less than 60% are shaded.

draft, resulting in θ increases in the lowest 1 km. The strongest warming is nearly 2 K just to the rear of the heaviest rainfall. Cooling results in a θ perturbation exceeding -3 K in two regions at 360 min (Fig. 21b). The more elevated of these regions is near the maximum of sublimation and melting. Warming aloft spreads rearward, with the greatest potential temperature increases, of over 4 K, occurring at 270 min rather close to the convective line. Cooling takes place above 9 km or so after 180 min due primarily to adiabatic cooling from the upward motion (Fritsch and Maddox 1981), although some weak sublimational cooling also occurs at these high levels.

These temperature perturbations result in hydrostatically induced mesoscale pressure perturbations (Fig. 22). Pressure is not a necessary variable for the integration of the model equations and is solved for here diagnostically using the hydrostatic relationship. The values of pressure shown in the figure are the deviations from the domain-averaged pressure. Because the domain is generally restricted to the stratiform region only, regions of high and low pressure should be considered relative to this area and not the larger-scale environment. At most times, a relative high in the pressure field occurs near the surface in the area of stratiform rain. At 180 min (Fig. 22a), the peak perturbation is around $+0.6$ mb. This peak reaches 1 mb at 270 min. By 360 min (Fig. 22b), the highest pressures at the surface are slightly rearward of the main rain region, and the maximum perturbation is around 1.5 mb. Regions of relatively low pressure occur at low and midlevels above the surface, with the strongest “me-

solow” at the back of the convective line. The ~ 1.2 -mb low near the convective line at 180 and 360 min (Figs. 22a, b) is strongest around the 2.5–3-km level. The low farther rearward is most intense near the melting level. The influence of this low pressure region expands with time. A weaker region of low pressure can be seen farther rearward near the back of the precipitation region at 180 min.

A pronounced surface wake low does not occur in this simulation, although there is a hint of slightly lower pressures near the back of the rain region at 180 min (Fig. 22a). This is the location of the well-pronounced mesolow observed in this case (Johnson and Hamilton 1988). The difference in pressure between the negative and positive perturbations toward the front of the rain region at these times is around 1 mb, which is less than half of the observed pressure difference on average over the stratiform region of the 10–11 June system. The failure of the model to reproduce a strong surface mesolow is probably linked to both relatively poor vertical resolution at low levels and the weakness of the RTF flow and descent at significant distances away from the convective line. Some of the weakness may be due to the neglect of ambient RTF flow in the initialization. The generation of intense wake lows will be explored in a subsequent paper.

f. Relative humidity

The strong FTR flow at middle and high levels quickly advects vapor across the domain (Fig. 23). Humidities with respect to water of over 90% approach

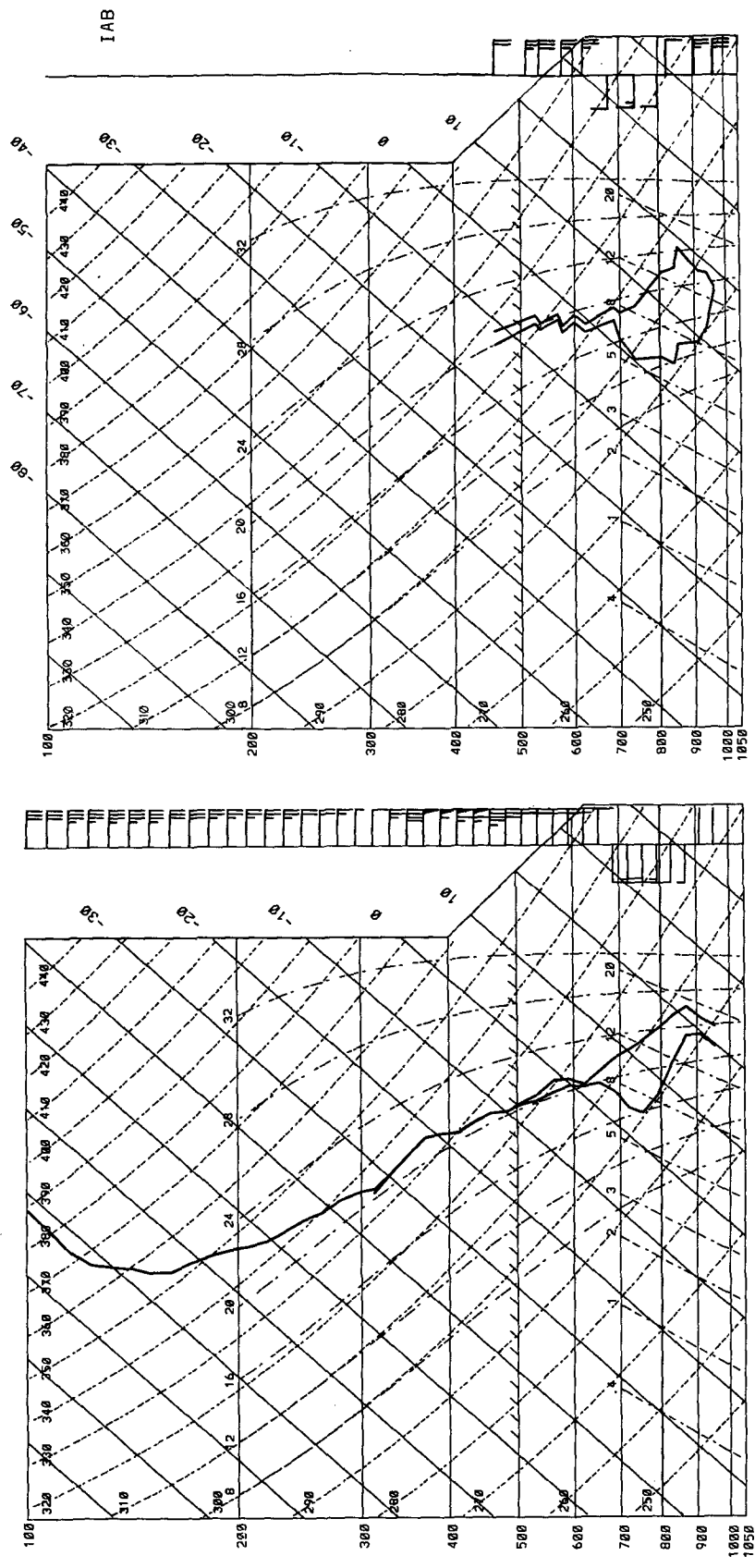


FIG. 24. Thermodynamic diagrams from (a) the region of heaviest stratiform rain in the model at 360 minutes and (b) Wichita, Kansas, at 0624 UTC.

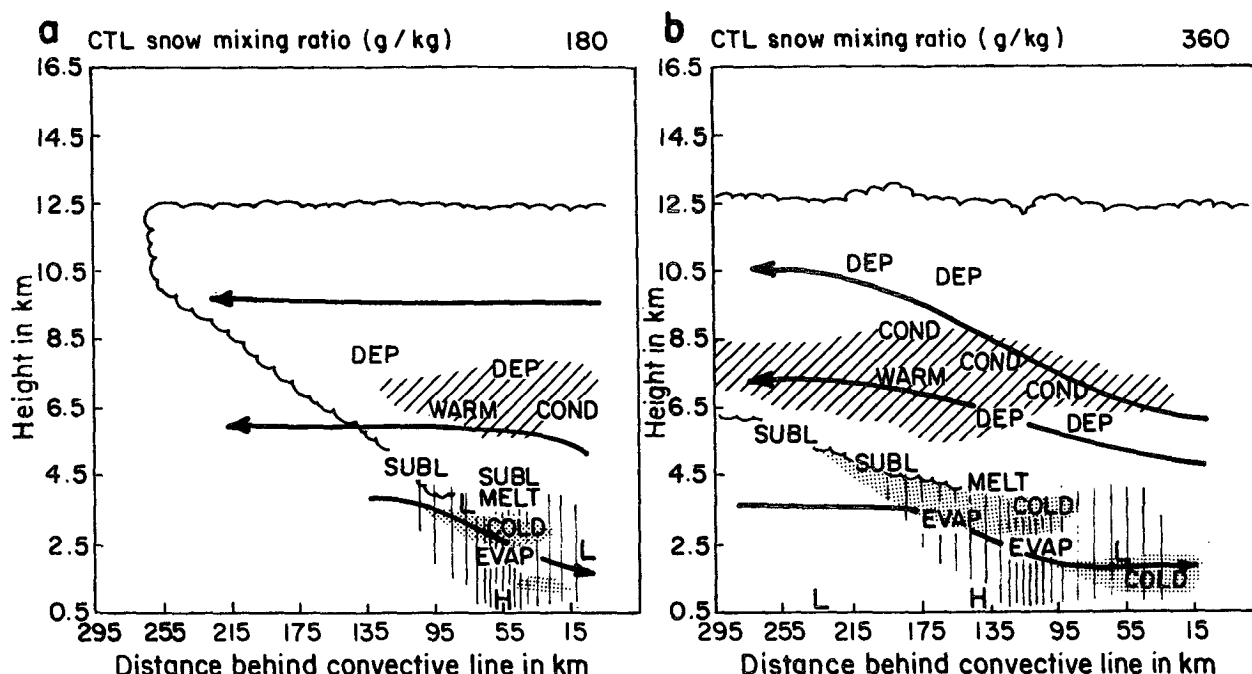


FIG. 25. Schematic depicting important kinematic, thermodynamic, and microphysical features during (a) the developing and (b) mature stages of the stratiform region.

the left boundary at 180 minutes (Fig. 23a). During the first 120 minutes of the simulation, dry air at midlevels retreats, but the strengthening rear-inflow jet begins transporting drier air back into the stratiform rain region at 180 minutes. Mesoscale descent also leads to drying in this region so that humidities drop below 55% after 270 minutes near the back of the surface rainfall at an elevation of 3 km (Fig. 23b). Generally, the minimum low-level humidities do not fall below 50% in the main rain region throughout the simulation. Soundings taken at later times in this relatively dry area (Fig. 24a) do show a hint of an "onion" structure (Zipser 1977). However, the greatest dewpoint depressions are found around the 800-mb level, somewhat higher than in typical onion soundings (Fig. 24b). The elevated dry region is probably due to the relatively coarse resolution of the model at low levels, 400 m.

5. Discussion

The two-dimensional cloud model used in this study produces features that reasonably agree with those observed in the stratiform region of the 10–11 June PRE-STORM squall line. The agreement indicates that the rather unique approach of restricting the domain to the stratiform region alone is acceptable if convective inputs are accurate. Rain intensity and vertical motions are rather weak during the first three hours of the stratiform region but increase significantly at later times. The rain area broadens with

time, and a transition zone grows markedly late in the simulation when the convective line is weakening. The rear-inflow jet develops first near the convective line and later expands several hundred kilometers rearward and intensifies. The jet descends markedly in the region of heaviest stratiform rainfall. The intensity of the jet is underestimated rearward of 50–100 km behind the convective line.

The important microphysical processes and kinematics both during the developing and mature stages of the stratiform region are depicted in Fig. 25. During the developing stages, ascent in the anvil cloud is weak, as implied by the streamlines. A current of rear-to-front flow forms relatively close to the convective line, and this current descends fairly significantly, even at this early stage of development, in the region of heaviest rainfall. A relatively warm region (1° – 3° C perturbation) develops at around the 6.5-km level in the anvil cloud, primarily caused by depositional heating. Sublimation is pronounced just above the melting level. Melting and evaporation result in significant cooling in the vicinity of the rear-inflow jet. The temperature perturbations result in a region of lower pressure that slopes from around the melting level at the rear of the rain region to about the 2.5-km level closer to the convective line. During the development of the system, the in situ production of condensate may contribute only 15% to the surface rainfall, and 70% of the condensate production is due to vapor deposition.

During maturity, in situ production of condensate becomes more important than advection from the convective line region, supplying over 65% of the surface rainfall. Vertical motions are strong and extensive, both in the anvil cloud and in the mesoscale downdraft below cloud base. Rainfall reaches the surface over a far larger area than at earlier times, and the heaviest rainfall is over 100 km rearward from the convective line. This is also the region of strongest ascent in the anvil cloud. Rear-to-front flow extends 300 km or more rearward of the convection, and the rear-inflow jet descends much faster in the area of heaviest rainfall than in other regions. Deposition is now important at high levels in the cloud (around 10.5 km), in addition to the 6–7-km layer. Condensation plays a much more important role at this time, supplying nearly three times as much condensate as deposition. The warm region covers a broad portion of the cloud. Sublimation is important all along the base of the cloud in the rear portion of the stratiform region. Melting and evaporation are significant over a large area at this time and again result in a cold anomaly along the rear-inflow jet. A midlevel mesolow continues and is strongest in the front portion of the stratiform region, at about the 2.5-km level. Surface high pressure in the rain region is followed by low pressure well behind the rain area.

Over the course of the entire simulation, in situ production of condensate contributes approximately 44% to the surface rainfall. This figure falls within the range given in water budget studies by Gamache and Houze (1983), Rutledge and Houze (1987), and GJ. An increase in the ascent at higher levels to better agree with

observations would result in better agreement of surface rainfall rates with observations and also in an increased percentage of in situ production so that the ratio might better agree with the 50% figure estimated for this case by GJ.

In summary, a dynamical and microphysical model has been developed and applied to the study of circulations within the trailing stratiform regions of squall lines. The input of hydrometeors to the stratiform region from the convective line was prescribed from observations and 1D modeling results. The 5-km horizontal resolution appeared to be sufficiently small to accurately simulate many features within the stratiform region, although in some systems where strong dynamics occur in the stratiform region, a smaller mesh size might be necessary. Most of the dynamics driving the model were due to ice processes, supporting previous conclusions (e.g., McCumber et al. 1991) that ice must be included in microphysical parameterizations for accurate depiction of MCSs.

Acknowledgments. The constructive comments of Prof. Steven Rutledge, Prof. Wayne Schubert, and Dr. Brad Smull were appreciated. The text was improved by the changes suggested by an anonymous reviewer. Some of the figures were expertly drafted by Judy Sorbie-Dunn. This research has been supported by a National Science Foundation graduate fellowship and National Science Foundation Grant ATM9013112, and final preparation of the paper was supported under the UCAR visiting scientist program at NMC.

APPENDIX A

List of Symbols

Symbols	Description	Value	SI units
a''	Constant in fallspeed relation for snow	12.37	$m^{(1-b)} s^{-1}$
a'''	Constant in fallspeed relation for graupel	8.73	$m^{(1-b')} s^{-1}$
b	Fallspeed exponent for snow	0.42	
b'	Fallspeed exponent for graupel	0.36	
c	Constant used in turbulence parameterization	0.5	
c_p	Specific heat of air at constant pressure	1004	$J kg^{-1} K^{-1}$
D	Constant used for horizontal exchange coefficient	5.0	
D_R	Raindrop diameter		m
f	Coriolis parameter		s^{-1}
g	Gravitational constant	9.8	$m s^{-2}$
J	Jacobian operator		
K_H	Horizontal eddy diffusivity of heat		$m^2 s^{-1}$
K_Z	Vertical eddy diffusivity of heat		$m^2 s^{-1}$
K_{Z0}	Constant background vertical eddy diffusivity of heat	0.6	$m^2 s^{-1}$
N_{0G}	Intercept value in graupel size distribution	4×10^6	m^{-4}
N_{0R}	Intercept value in raindrop size distribution	8×10^6	m^{-4}
N_{0S}	Intercept value in snowflake size distribution	4×10^6	m^{-4}
p	Pressure		$N m^{-2}$

Symbols	Description	Value	SI units
p_0	Reference pressure	100 000	N m^{-2}
Q^*	Diabatic heating term		$\text{K kg m}^{-3} \text{s}^{-1}$
q_g	Mixing ratio of graupel		kg kg^{-1}
q_r	Mixing ratio of rainwater		kg kg^{-1}
q_s	Mixing ratio of snow		kg kg^{-1}
S_0	Represents sources and sinks for q		$\text{kg m}^{-3} \text{s}^{-1}$
T	Temperature		K
T_0	Reference temperature	273.16	K
t	Time		s
u	Horizontal x -velocity perturbation		m s^{-1}
$U(z)$	Basic x velocity		m s^{-1}
v	y velocity		m s^{-1}
\bar{V}	Mass-weighted fallspeed of precipitation		m s^{-1}
\bar{V}_G	Mass-weighted fallspeed for graupel		m s^{-1}
\bar{V}_R	Mass-weighted fallspeed for rain		m s^{-1}
\bar{V}_S	Mass-weighted fallspeed for snow		m s^{-1}
w	Vertical air velocity		m s^{-1}
x	Horizontal distance		m
z	Vertical distance		m
α	Specific volume of air		$\text{m}^3 \text{kg}^{-1}$
α_0	Reference specific volume		$\text{m}^3 \text{kg}^{-1}$
ρ	Air density		kg m^{-3}
ρ_G	Density of graupel	400	kg m^{-3}
ρ_L	Density of water	1000	kg m^{-3}
ρ_S	Density of snow	100	kg m^{-3}
λ_G	Slope of graupel size distribution		m^{-1}
λ_R	Slope of raindrop size distribution		m^{-1}
λ_S	Slope of snow size distribution		m^{-1}
η	Vorticity in the x - z plane		s^{-2}
ν_H	Horizontal eddy viscosity		$\text{m}^2 \text{s}^{-1}$
ν_Z	Vertical eddy viscosity		$\text{m}^2 \text{s}^{-1}$
ψ	Streamfunction in the x - z plane		$\text{kg s}^{-1} \text{m}^{-1}$
θ	Potential temperature		K
θ_0	Reference potential temperature		K
Δt	Time increment	15	s
Δx	Horizontal spatial increment	5000	m
Δz	Vertical spatial increment	400	m

APPENDIX B

Microphysical Parameterization

The microphysical parameterization used in this model is the six water class scheme used by Rutledge and Hobbs (1983, 1984), which is similar to the parameterization described in Lin et al. (1983). Minor modifications have been made to these schemes, including the corrections to the snow and graupel fallspeeds discussed in Potter (1991). The detailed scheme can be found in Rutledge and Hobbs and will not be presented here.

a. Slope factors

The slope factors, as in Rutledge and Hobbs (1983, 1984) but with modifications to agree with Locatelli

and Hobbs (1974) and as presented in Potter (1991), are

$$\lambda_R = \left(\frac{\alpha \pi \rho_L N_{0R}}{q_r} \right) \quad (\text{A1})$$

$$\lambda_S = \left(\frac{\alpha \pi \rho_L N_{0S}}{q_s} \right) \quad (\text{A2})$$

$$\lambda_G = \left(\frac{\alpha \pi \rho_L N_{0G}}{q_g} \right), \quad (\text{A3})$$

where α is the specific volume.

b. Mass-weighted fallspeeds

All hydrometeors in the precipitating fields are assumed to fall at their mass-weighted fallspeeds. For

rain, the polynomial fit used in Rutledge and Hobbs (1983),

$$V_R(D_R) = -0.267 + 51.5D_R - 102.25D_R^2 + 75.5D_R^3, \quad (A4)$$

determines the fallspeed, where D_R is in centimeters and V_R is in meters per second. Making appropriate substitutions, the equation becomes

$$\bar{V}_R = (-0.267 + 206\lambda_R^{-1} - 2.045 \times 10^3\lambda_R^{-2} + 9.06 \times 10^3\lambda_R^{-3}) \left(\frac{p_0}{p} \right)^{0.4}, \quad (A5)$$

where λ_R (cm^{-1}) is given by Eq. (A1).

The fallspeed equation for snow is derived similarly to Rutledge and Hobbs (1983) and is

$$\bar{V}_S = a'' \frac{\Gamma(4+b)}{6} \lambda_S^{-b} \left(\frac{p_0}{p} \right)^{0.4}, \quad (A6)$$

where λ_S is given by Eq. (A2), and the values of a'' and b as shown in appendix A differ from those previously used by Lin et al. (1983) and Rutledge and Hobbs (1983) because of corrections suggested by Potter (1991).

The fallspeed equation for graupel is derived as in Rutledge and Hobbs (1984) and is

$$\bar{V}_G = a''' \frac{\Gamma(4+b')}{6} \lambda_G^{-b'} \left(\frac{p_0}{p} \right)^{0.4}, \quad (A7)$$

where λ_G is given by Eq. (A3), and a''' and b' (see appendix A) are adjusted (Potter 1991) from the values used in Rutledge and Hobbs (1984).

REFERENCES

- Arakawa, A., 1966: Computational design for long-term numerical integration of the equations of fluid motion: Two-dimensional incompressible flow, Part I. *J. Comput. Phys.*, **1**, 119–143.
- Asselin, R., 1972: Frequency filter for time integrations. *Mon. Wea. Rev.*, **100**, 487–490.
- Biggerstaff, M. I., and R. A. Houze, Jr., 1993: Kinematics and microphysics of the transition zone of the 10–11 June 1985 squall line. *J. Atmos. Sci.*, **50**, 3091–3110.
- Bluestein, H. B., and M. H. Jain, 1985: Formation of mesoscale lines of precipitation: Severe squall lines in Oklahoma during the spring. *J. Atmos. Sci.*, **42**, 1711–1732.
- Bott, A., 1989: A positive definite advection scheme obtained by nonlinear renormalization of the advective fluxes. *Mon. Wea. Rev.*, **117**, 1006–1015.
- Chong, M., and D. Hauser, 1990: A tropical squall line observed during the COPT 81 experiment in West Africa. Part III: Heat and moisture budgets. *Mon. Wea. Rev.*, **118**, 1696–1706.
- , P. Amayenc, G. Scialom, and J. Testud, 1987: A tropical squall line observed during the COPT 81 experiment in West Africa. Part I: Kinematic structure inferred from dual Doppler radar data. *Mon. Wea. Rev.*, **115**, 670–694.
- Churchill, D. D., and R. A. Houze, Jr., 1984: Development and structure of winter monsoon cloud clusters on 10 December 1978. *J. Atmos. Sci.*, **41**, 933–960.
- Cotton, W. R., and R. A. Anthes, 1989: *Storm and Cloud Dynamics*. Academic Press, 883 pp.
- Dudhia, J., M. W. Moncrieff, and D. W. K. So, 1987: The two-dimensional dynamics of West African squall lines. *Quart. J. Roy. Meteor. Soc.*, **113**, 121–146.
- Durran, D. R., M.-J. Yang, D. N. Slinn, and R. G. Brown, 1993: Toward more accurate wave-permeable boundary conditions. *Mon. Wea. Rev.*, **121**, 604–620.
- Ferrier, B. S., and R. A. Houze, Jr., 1989: One-dimensional time-dependent modeling of GATE cumulonimbus convection. *J. Atmos. Sci.*, **46**, 330–352.
- Fovell, R. G., 1991: Influence of the Coriolis force on two-dimensional model storms. *Mon. Wea. Rev.*, **119**, 606–630.
- , and Y. Ogura, 1988: Numerical simulations of a mid-latitude squall line in two dimensions. *J. Atmos. Sci.*, **45**, 3846–3879.
- Fritsch, J. M., and R. A. Maddox, 1981: Convectively driven mesoscale pressure systems aloft. Part I: Observations. *J. Appl. Meteor.*, **20**, 9–19.
- Gallus, W. A., Jr., and R. H. Johnson, 1991: Heat and moisture budgets of an intense midlatitude squall line. *J. Atmos. Sci.*, **48**, 122–146.
- , and —, 1992: The momentum budget of an intense midlatitude squall line. *J. Atmos. Sci.*, **49**, 422–450.
- Gamache, J. F., and R. A. Houze, 1982: Mesoscale air motions associated with a tropical squall line. *Mon. Wea. Rev.*, **110**, 118–135.
- , and —, 1983: Water budget of a mesoscale convective system in the tropics. *J. Atmos. Sci.*, **40**, 1835–1850.
- Heymsfield, A. J., and M. R. Hjermfelt, 1984: Processes of hydrometeor development in Oklahoma convective clouds. *J. Atmos. Sci.*, **41**, 2811–2835.
- Houze, R. A., Jr., 1982: Cloud clusters and large-scale vertical motions in the tropics. *J. Meteorol. Soc. Japan*, **60**, 396–409.
- Hsie, E.-Y., R. A. Anthes, and D. Keyser, 1984: Numerical simulation of frontogenesis in a moist atmosphere. *J. Atmos. Sci.*, **41**, 2581–2594.
- Johnson, R. H., and P. J. Hamilton, 1988: The relationship of surface pressure features to the precipitation and air flow structure of an intense midlatitude squall line. *Mon. Wea. Rev.*, **116**, 1444–1472.
- , W. A. Gallus, Jr., and M. D. Vescio, 1990: Near-tropopause vertical motions within the trailing stratiform regions of squall lines. *J. Atmos. Sci.*, **47**, 2200–2210.
- Klimowski, B. A., 1994: Initiation and development of rear inflow within the June 28–29 North Dakota mesoconvective system. *Mon. Wea. Rev.*, **122**, 765–779.
- Knupp, K. R., and W. R. Cotton, 1987: Internal structure of a small mesoscale convective system. *Mon. Wea. Rev.*, **115**, 629–645.
- LaFore, J.-P., and M. W. Moncrieff, 1989: A numerical investigation of the organization and interaction of the convective and stratiform regions of tropical squall lines. *J. Atmos. Sci.*, **46**, 521–524.
- Leary, C. A., and R. A. Houze, Jr., 1979: Melting and evaporation of hydrometeors in precipitation from the anvil clouds of deep tropical convection. *J. Atmos. Sci.*, **36**, 669–679.
- , and E. N. Rappaport, 1987: The life cycle and internal structure of a mesoscale convective complex. *Mon. Wea. Rev.*, **115**, 1503–1527.
- LeMone, M. A., 1983: Momentum transport by a line of cumulonimbus. *J. Atmos. Sci.*, **40**, 1815–1834.
- Lin, Y.-L., R. D. Farley, and H. D. Orville, 1983: Bulk parameterization of the snow field in a cloud model. *J. Climate Appl. Meteor.*, **22**, 1065–1092.
- Locatelli, J. D., and P. V. Hobbs, 1974: Fall speeds and masses of solid precipitation particles. *J. Geophys. Res.*, **79**, 2185–2197.
- Matejka, T., and T. J. Schuur, 1991: The relationship between vertical air motions and the precipitation band in the stratiform region of a squall line. Preprints, *25th Int. Conf. on Radar Meteorology*, Paris, Amer. Meteor. Soc., 501–504.
- McCumber, M., W.-K. Tao, J. Simpson, R. Penc, and S.-T. Soong, 1991: Comparison of ice phase microphysical parameterization schemes using numerical simulations of tropical convection. *J. Appl. Meteor.*, **30**, 985–1004.

- Newton, C. W., 1950: Structure and mechanisms of the prefrontal squall line. *J. Meteor.*, **7**, 210–223.
- Ogura, Y., and N. A. Phillips, 1962: Scale analysis of deep and shallow convection in the atmosphere. *J. Atmos. Sci.*, **19**, 173–179.
- , and M.-T. Liou, 1980: The structure of a midlatitude squall line: A case study. *J. Atmos. Sci.*, **37**, 553–567.
- Orlanski, I., 1976: A simple boundary condition for unbounded hyperbolic flows. *J. Comput. Phys.*, **21**, 251–269.
- , and B. B. Ross, 1973: Numerical simulation of the generation and breaking of internal gravity waves. *J. Geophys. Res.*, **78**, 8808–8826.
- , and —, 1977: The circulation associated with a cold front. Part I: Dry case. *J. Atmos. Sci.*, **33**, 1619–1633.
- Potter, B. E., 1991: Improvements to a commonly used cloud microphysical bulk parameterization. *J. Appl. Meteor.*, **30**, 1040–1042.
- Redelsberger, J. L., and J. P. LaFore, 1988: A three-dimensional simulation of a tropical squall line: Convective organization and thermodynamic vertical transport. *J. Atmos. Sci.*, **45**, 1334–1356.
- Rickenbach, T. M., 1990: Precipitation processes and water budget study of the 10–11 June 1985 mesoscale convective system. M. S. thesis, Colorado State University, 180 pp. [Available from Atmos. Sci. Dept., Colorado State University, Ft. Collins, CO, 80523.]
- Roux, F., 1988: The West African squall line observed on 23 June 1981 during COPT 81: Kinematics and thermodynamics of the convective region. *J. Atmos. Sci.*, **45**, 406–426.
- Rutledge, S. A., 1986: A diagnostic numerical study of the stratiform region associated with a tropical squall line. *J. Atmos. Sci.*, **43**, 1337–1358.
- , and P. V. Hobbs, 1983: The mesoscale and microscale structure and organization of clouds and precipitation in midlatitude cyclones. VIII: A model for the “Seeder–Feeder” process in warm-frontal rainbands. *J. Atmos. Sci.*, **40**, 1185–1206.
- , and —, 1984: The mesoscale and microscale structure and organization of clouds and precipitation in midlatitude cyclones. XII: A diagnostic modeling study of precipitation development in narrow cold-frontal rainbands. *J. Atmos. Sci.*, **41**, 2949–2972.
- , and R. A. Houze, Jr., 1987: A diagnostic modeling study of the trailing stratiform region of a midlatitude squall line. *J. Atmos. Sci.*, **44**, 2640–2656.
- , and D. R. MacGorman, 1988: Cloud-to-ground lightning activity in the 10–11 June 1985 mesoscale convective system observed during the Oklahoma–Kansas PRE-STORM project. *Mon. Wea. Rev.*, **116**, 1393–1408.
- , R. A. Houze, Jr., M. I. Biggerstaff, and T. Matejka, 1988: The Oklahoma–Kansas mesoscale convective system of 10–11 June 1985: Precipitation structure and single-Doppler radar analysis. *Mon. Wea. Rev.*, **116**, 1409–1430.
- Schmidt, J. M., and W. R. Cotton, 1990: Interactions between upper and lower atmospheric gravity waves on squall line structure and maintenance. *J. Atmos. Sci.*, **47**, 1205–1222.
- Smull, B. F., and R. A. Houze, 1985: A midlatitude squall line with a trailing region of stratiform rain: Radar and satellite observations. *Mon. Wea. Rev.*, **113**, 117–133.
- , and —, 1987a: Dual-Doppler radar analysis of a midlatitude squall line with a trailing region of stratiform rain. *J. Atmos. Sci.*, **43**, 356–377.
- , and —, 1987b: Rear inflow in squall lines with trailing stratiform precipitation. *Mon. Wea. Rev.*, **115**, 2869–2889.
- Srivastava, R. C., T. J. Matejka, and T. J. Lorello, 1986: Doppler radar study of the trailing anvil region associated with a squall line. *J. Atmos. Sci.*, **43**, 356–377.
- Stensrud, D. J., R. A. Maddox, and C. L. Ziegler, 1991: A sublimation-initiated mesoscale downdraft and its relation to the wind field below a precipitating anvil cloud. *Mon. Wea. Rev.*, **119**, 2124–2139.
- Stumpf, G. J., R. H. Johnson, and B. F. Smull, 1991: The wake low in a midlatitude mesoscale convective system having complex convective organization. *Mon. Wea. Rev.*, **119**, 134–158.
- Szeto, K. K., C. A. Lin, and R. E. Stewart, 1988a: Mesoscale circulations forced by melting snow. Part I: Basic simulations and dynamics. *J. Atmos. Sci.*, **45**, 1629–1641.
- , R. E. Stewart, and C. A. Lin, 1988b: Mesoscale circulations forced by melting snow. Part II: Application to meteorological features. *J. Atmos. Sci.*, **45**, 1642–1650.
- Tao, W.-K., and J. Simpson, 1989: Modeling study of a tropical squall-type convective line. *J. Atmos. Sci.*, **46**, 177–202.
- , —, and S.-T. Soong, 1991: Numerical simulation of a subtropical squall line over the Taiwan Strait. *Mon. Wea. Rev.*, **119**, 2699–2723.
- , —, C.-H. Sui, B. Ferrier, S. Lang, J. Scala, M.-D. Chou, and K. Pickering, 1993: Heating, moisture, and water budgets of tropical and midlatitude squall lines: Comparison and sensitivity to longwave radiation. *J. Atmos. Sci.*, **50**, 673–690.
- Webster, P. J., and G. L. Stephens, 1980: Tropical upper-tropospheric extended clouds: Inferences from winter MONEX. *J. Atmos. Sci.*, **37**, 1521–1541.
- Weisman, M. L., 1992: The role of convectively generated rear-inflow jets in the evolution of long-lived mesoconvective systems. *J. Atmos. Sci.*, **49**, 1826–1847.
- Willis, P. T., and A. J. Heymsfield, 1989: Structure of the melting layer in mesoscale convective system stratiform precipitation. *J. Atmos. Sci.*, **46**, 2008–2025.
- Zhang, D.-L., and K. Gao, 1989: Numerical simulation of an intense squall line during 10–11 June 1985 PRE-STORM. Part II: Rear inflow, surface pressure perturbations, and stratiform precipitation. *Mon. Wea. Rev.*, **117**, 2067–2094.
- , —, and D. B. Parsons, 1989: Numerical simulation of an intense squall line during 10–11 June 1985 PRE-STORM. Part I: Model verification. *Mon. Wea. Rev.*, **117**, 960–994.
- Zipper, E. J., 1969: The role of organized unsaturated convective downdrafts in the structure and rapid decay of an equatorial disturbance. *J. Appl. Meteor.*, **8**, 799–814.
- , 1977: Mesoscale and convective-scale downdrafts as distinct components of squall-line structure. *Mon. Wea. Rev.*, **105**, 1568–1589.